Check for updates

Novel metallated imidazole phthalocyanines: synthesis, ultrafast excited-state carrier dynamics and multiphoton absorption properties†

Md Soif Ahmed, [iD] [a] Kalavala Shivaprakash Srivishnu, [iD] [bc] Chinmoy Biswas,[a] Dipanjan Banerjee,[e] Prabhakar Chetti,[d] Venugopal Rao Soma,[e] Lingamallu Giribabu [iD] *[bc] and Sai Santosh Kumar Raavi [iD] *[af]

Metal-substituted phthalocyanines are an important class of materials garnering attention due to their structural diversity and excellent optoelectronic properties. Herein, we comprehensively investigate the photophysical properties of a newly synthesized metal-free and metallated [Zn(II) and Cu(II)] phthalocyanines (Pcs) to explore their nonlinear optical (NLO) phenomena. Femtosecond transient absorption spectroscopy (fs-TAS) was utilized to study the excited-state relaxation dynamics of these Pcs within the visible spectral range of 430–780 nm. After photoexcitation, fs-TAS data confirmed the formation of long-lived triplet states due to intersystem crossing. The lifetimes of various intermediate excited states were retrieved from the TAS data using a target model analysis, and these lifetime values were used to fit the NLO data, which were carried out by the femtosecond Z-scan measurements. The calculated nonlinear refractive indices were $(0.36-0.68) \times 10^{-15}$ cm^2 W^{-1} and the values of second hyperpolarizability were $(2.34-3.61) \times 10^{-30}$ esu for these Pcs, which were verified through DFT calculations. Compared with the metal-free Pc, an enhancement of the nonlinear characteristics for the metallated Pcs was observed, and we attributed this increment to the reduction of aggregation for the metallated Pcs replaced with organic scaffolds at their peripheral locations. As a proof-of-concept application, we calculated the optical limiting onset and figure of merit. The crucial photophysical and nonlinear phenomena obtained here are believed to provide the avenues to address the critical variables involved and their correlated optoelectronic properties.

Introduction

Ultrafast electron transfer (ET) through photoexcitation in systems that involve a donor and an acceptor has contributed greatly to the advancement of various fields such as nonlinear optics, artificial photosynthesis, optoelectronic conversion, and solar energy harvesting technologies.[1–5] The successful matching of a donor and an acceptor that possess the necessary photophysical and electrochemical parameters is crucial for achieving an exothermic ET process. Porphyrins, phthalocyanines (Pcs), fullerenes (C60, C70), and perylene bisimide dyes, which have exceptional structural flexibility as well as electrical and optoelectronic capabilities, are used to develop supramolecular D–A systems that can be used to develop organic/polymeric solar cells[6] and nonlinear optical (NLO) devices.[7]

Phthalocyanines, which are planar cyclic organic compounds with an 18-π-electron tetrapyrrolic structure, demonstrate substantial reverse saturable absorption (RSA) owing to multiphoton absorption (MPA) and are considered to be one of the most versatile and strong organic NLO materials because of their extended 18-π-electron system in two dimensions.[8] Significant advancements have been achieved in nonlinear optics over the past two decades due to the significance and application of NLO in photonics, optical switching, optical limiting, and optoelectronics.[9–12] Incorporating a variety of substituents at the peripheral and axial parts, with various

[a] Ultrafast Photophysics and Photonics Laboratory, Department of Physics, Indian Institute of Technology Hyderabad, Kandi 502285, Telangana, India.
E-mail: sskraavi@phy.iith.ac.in

[b] Polymers & Functional Materials Division, CSIR-Indian Institute of Chemical Technology, Tarnaka, Hyderabad-500007, India. E-mail: giribabu@iict.res.in

[c] Academy of Scientific and Innovative Research (AcSIR), Ghaziabad-201002, India

[d] Department of Chemistry, National Institute of Technology, Kurukshetra 136119, India

[e] Advanced Centre of Research in High Energy Materials (ACRHEM), DRDO Industry Academia – Centre of Excellence (DIA-COE), University of Hyderabad, Hyderabad 500046, Telangana, India

[f] Department of Climate Change, Indian Institute of Technology Hyderabad, Kandi 502285, Telangana, India

† Electronic supplementary information (ESI) available. See DOI: https://doi.org/10.1039/d3ma00225j

options for changing the substitution pattern in terms of the quantity and location, significantly impacts the linear absorption spectra and NLO properties of Pcs. In addition, the crystal structure of the compound and the π-electron conjugation influence the optical nonlinearities. Moreover, a strong dipole moment can develop due to the asymmetry in a phthalocyanine, resulting in higher order nonlinearity.[13] However, one of the main disadvantages of Pcs is that, due to the aggregation effect,[14] most are not soluble in common organic solvents. Several research groups, including our group, have synthesized metal-substituted phthalocyanines by inserting alkoxy or bulky alkyl groups at non-peripheral or peripheral sites.[15,16] Metallophthalocyanines with heavy metal ions such as Pb, Cu, and Zn at their core exhibit a persistent perpendicular dipole moment relative to the phthalocyanine plane, and their nonlinear properties are enhanced via spin–orbit coupling. Organic scaffolds such as imidazoles, indoles, and carbazoles can replace the peripheral positions of metallated phthalocyanines, reducing aggregation and providing an easy way to adjust the optoelectronic properties of the Pc's macrocycle. Since the dipole moments of axially substituted Pcs are perpendicular to the Pc's macrocycle, they result in a weak aggregation effect and, eventually, these Pcs demonstrate a substantially larger NLO response.[17]

Understanding the structural–photophysical interactions of metal-substituted Pc complexes through theory and experiments is of significant interest in producing optimized Pc designs with improved optical properties. Understanding the light absorption, emission, triplet yield, and MPA of these Pcs is crucial for both linear and nonlinear optics. By contrast, as D–A metallated Pc systems are believed to have an effective charge transfer pathway, they are excellent for use in photovoltaics, photocatalysis, bio-imaging and biomedicine. Therefore, understanding the ultrafast excited-state carrier dynamics of such compounds is essential for basic as well as applied sciences. Applications of phthalocyanines are associated with electronic transitions that occur across a broad spectral range, including the B-band and the Q-band transitions. Recent photophysical investigations have focused on the absorption characteristics of excited singlet or triplet states.[18,19] Metallated Pcs are highly sought-after for their photophysical behavior that involves the transfer of electrons from singlet to triplet states upon excitation of the Soret band, which is referred to as intersystem crossing (ISC). After Soret band excitation, the relaxation process in the Pc molecule within the range of excited states takes place within a few hundred femtoseconds. Despite extensive research on the excited-state properties of several Pc derivatives, there is a scarcity of comprehensive investigations into the rate constants and decay lifetimes of various excited-state species of novel Pcs. Furthermore, correlating the decay rate constants with NLO applications by utilizing the rate constants to obtain different NLO parameters of phthalocyanines is not found in earlier reports.

Many replacement techniques have been developed over time to enhance the conjugation duration of central phthalocyanine cores and to achieve photochemical stability, a higher triplet yield and a greater MPA cross-section. Due to the

presence of delocalized π-electrons, higher nonlinear parameters were expected and the Pc molecules demonstrated excellent nonlinear optical properties. Liu et al.[20] have studied the NLO properties of phthalocyanine F_{16}PcGa-BP in PMMA using the Z-scan method with a 532 nm nanosecond (ns) laser where RSA with a two-photon absorption coefficient (β) of 282.86 cm GW^{-1} was reported at the incident laser energy of 400 μJ. Mwanza et al.[21] found that adding cobalt (Co) and manganese (Mn) to the ring of Pcs with a 4-(propargyloxy)phenoxy group led to a decrease in the nonlinear response in comparison with the free-base Pc, and they obtained β values of 14.3, 9.20 and 23.5 cm GW^{-1} using the nanosecond Z-scan method for Co, Mn and free-base Pc, respectively. β values of 2.71, 2.37 and 2.04 cm GW^{-1} were obtained, respectively, for lanthanum, holmium and ytterbium central-atom-based polymeric carboxyl Pcs using a picosecond (ps) 532 nm laser by Zhao et al.[22] Our group has obtained the NLO properties of novel Pc systems employing femtosecond (fs) Z-scan experiments,[8,18,23,24] unveiling the exotic photonic responses in the nonlinear domain. In the present work, we studied comprehensively the photophysical properties and the fs Z-scan measurements of a newly synthesized metal-free Pc (H_2-TIPc) and its metallated derivatives, i.e., Zn(II) (Zn-TIPc) and Cu(II) (Cu-TIPc) (see Fig. 1) toward NLO applications. The optimized structures of individual Pc systems were obtained using DFT/TD-DFT calculations, and it was found that the theoretical outcomes were in agreement with the experimental observations. With other photophysical characterizations such as absorption, photoluminescence (PL), time-resolve PL (TRPL) and spectroelectrochemical studies, we
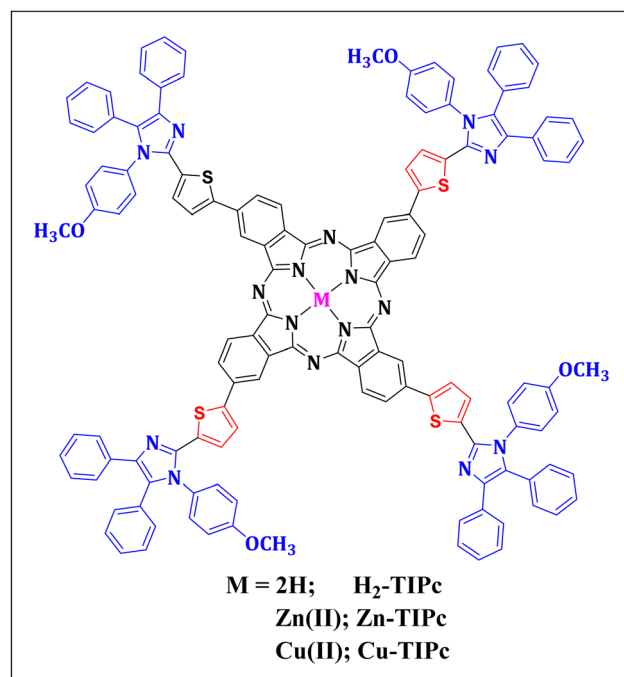

Fig. 1 Molecular structure of newly synthesized phthalocyanines. The free-base (or core-metal-free) phthalocyanine is represented by H_2-TIPc; Zn(II) and Cu(II) metallated derivatives are represented by Zn-TIPc, and Cu-TIPc, respectively.

thoroughly investigated the ultrafast photogenerated intermediate states with the aid of global and target model analysis of fs-TAS data. Femtosecond-TAS confirmed the occurrence of inter-system crossing and revealed a longer decay time of triplet-state excitons, which is favorable for increasing the carrier diffusion length *via* the triplet sensitization pathway. Notably, a very high triplet lifetime was observed for Cu-TIPc, and we explained that the improvement in molecular interaction, the increase in the Förster energy transfer process and the formation of a distinct tripdoublet state (also supported with DFT calculations) are the causes of the divergence of the Cu-based Pc's decay curves. The obtained decay rate constants of different excited states from fs-TAS have been utilized to fit the open-aperture Z-scan data implementing the three-level model. Both the two-photon absorption (2PA) and three-photon absorption (3PA) coefficients were obtained simultaneously, and the calculated NLO parameters are all high and are better compared with the NLO parameters reported for similar material systems. In addition, we investigated two important NLO applications, *i.e.*, the figure of merit (FOM) and the optical limiting onset, which indicate the potential use of these Pc material systems in nonlinear optoelectronic devices.

Experimental details

Materials

The reagents and chemicals used in the experiments were purchased from a commercial supplier, Merck, Sigma-Aldrich, and were subjected to additional purification processes. Laboratory reagent (LR) grade solvents were utilized for the purposes of both purification and column chromatography. The entire process was carried out in an inert atmosphere using solvents that were dry and degassed.

Synthesis of (5-(1-(4-methoxyphenyl)-4,5-diphenyl-1*H*-imidazol-2-yl)thiophen-2-yl) boronic acid (ThIm). For the chemical reaction, a 250 mL round-bottomed flask was prepared by ensuring its cleanliness and dryness. Inside the flask, 500 mg of benzil (equivalent to 2.38 mmol), 371 mg of 5-formyl-2-thiophene-boronic acid (equivalent to 2.38 mmol), 439 mg of *p*-anisidine (equivalent to 3.57 mmol), and 916.3 mg of ammonium acetate (equivalent to 11.9 mmol) were dissolved in 30 mL of acetic acid. After nitrogen degassing, the mixture was stirred for 24 hours at 90 °C in an inert atmosphere. Later, the reaction mixture was dried under reduced pressure after cooling. Ethyl acetate and water were used for extraction of the mixture, and the organic phase was purified using Na_2SO_4. Furthermore, the solvent was evaporated under reduced pressure at 50 °C, and the remaining substance was purified *via* silica gel column chromatography with a 10 : 1 ratio of hexane–ethyl acetate. A 65% yield was noted. Anal. Calcd for $C_{26}H_{21}BN_2O_3S$: C, 69.04; H, 4.68; N, 6.19%. Found: C, 69.00; H, 4.71; N, 6.20%. ^{1}H NMR (400 MHz, CDCl₃) δ 7.59 (2H, d, *J* 7.4), 7.24–7.21 (4H, m), 7.20 (2H, d, *J* 7.4), 7.16 (2H, d, *J* 4.8), 7.13–7.11 (2H, d, *J* 4.8), 6.88–6.84 (3H, m), 6.75 (1H, d), 3.81 (3H, s). Melting point (MP): 204 °C.

Synthesis of 4-(5-(1-(4-methoxyphenyl)-4,5-diphenyl-1*H*-imida-zol-2-yl)thiophen-2-l)phthalonitrile (TIPn). TIPn was synthesized by combining (5-(1-(4-methoxyphenyl)-4,5-diphenyl-1*H*-imidazol-2-yl)thiophen-2-yl)boronic acid, 4-iodophthalonitrile, and [1,1′-bis-(diphenylphosphino)ferrocene]palladium(II)dichloride in a round-bottomed flask containing toluene and THF. The mixture was purged with nitrogen for 15 minutes, and then a solution of 2 M Na_2CO_3 was added using a syringe under an inert atmosphere. The reaction mixture was purged again for 30 minutes and stirred at reflux temperature for 4 hours. Afterward, the mixture was cooled to temperature, dried using decreased pressure, and extracted using a combination of ethyl acetate and water. The yield obtained through silica gel column chromatography using hexane and ethyl acetate (3 : 1) was 51%. Anal. Calcd for $C_{34}H_{22}N_4OS$: C, 76.38; H, 4.15; N, 10.48%. Found: C, 76.41; H, 4.18; N, 10.50%. MALDI-TOF (*m/z*) = 534.63 (calculated mass = 535.08). ^{1}H-NMR (CDCl₃, 500 MHz, TMS) δ (ppm) = 7.88 (1H, d), 7.82 (2H, m), 7.76 (2H, m), 7.57 (2H, d, *J* 7.4), 7.27 (2H, d, *J* 7.4), 7.24 (2H, d), 7.21 (1H, s), 7.17 (4H, m), 6.92 (2H, d), 6.80 (1H, d), 3.85 (3H, s). MP: 264 °C.

Synthesis of H_2-TIPc. To start the process, 500 mg (0.93 mmol) of **TIPn** was dissolved in 5 ml of *n*-pentanol in a round-bottomed flask of 25 mL. The mixture was stirred for 15 minutes at a temperature of 150 °C, and then a catalytic amount of Li-metal was added. The color of the mixture changed from yellow to dark green, and stirring was continued under a nitrogen atmosphere for 6 hours. To perform the de-lithiation reaction, the contents of the flask were brought to room temperature, and a few drops of concentrated HCl were added, followed by stirring for 4 hours to remove the Li metal. The resulting mixture was extracted with water and dichloromethane, and the solvent was evaporated under reduced pressure. The remaining substance was then purified using silica gel column chromatography with dichloromethane as eluent, and the green band was collected to obtain a yield of 35%. Anal. Calcd for $C_{136}H_{90}N_{16}O_4S_4$: C, 76.31; H, 4.24; N, 10.47%. Found: C, 76.41; H, 4.22; N, 10.50%. MALDI-TOF (*m/z*) $C_{136}H_{90}N_{16}O_4S_4$: 2139.69 (Calculated mass: 2139.62). IR (in cm⁻¹): 3423, 2925, 1501, 1443, 1102, 615. MP: >300 °C.

Synthesis of Zn-TIPc. In a sterile round-bottomed flask, 50 mg of H_2-TIPc (0.023 mmol) was dissolved in 10 mL of DMF. To this mixture, 48 mg of zinc acetate (0.15 mmol) was added and stirred for four hours at 150 °C under an inert atmosphere. After completion, the crude product was poured onto ice, extracted with DCM, washed with water, and dried over Na_2SO_4. The product was then subjected to purification using silica gel column chromatography, with DCM : MeOH (90 : 10) as the eluent. The resulting yield was 30%. Anal. Calcd for $C_{136}H_{88}N_{16}O_4S_4Zn$: C, 74.12; H, 4.02; N, 10.17%. Found: C, 74.10; H, 4.05; N, 10.20%. MALDI-TOF (*m/z*) $C_{136}H_{80}N_{16}O_4S_4Zn$: 2204.04 (Calculated mass: 2203.93). IR (in cm⁻¹): 3422, 2924, 1600, 1404, 1101, 618. MP: >300 °C.

Synthesis of Cu-TIPc. We adopted a similar synthetic procedure to Zn-TIPc, where the only difference is that we used cupper acetate instead of zinc acetate. The crude compound was purified using silica gel column chromatography using DCM : MeOH (90 : 10). The yield was observed to be 35%. Anal. Calcd for $C_{136}H_{80}N_{16}O_4S_4Cu$: C, 74.18; H, 4.03; N, 10.18%. Found: C, 74.20; H, 4.05; N, 10.21%. MALDI-TOF (*m/z*) $C_{136}H_{80}N_{16}O_4S_4Cu$: 2202.94 (Calculated mass: 2202.09). IR (in cm⁻¹): 3421, 2920, 1580, 1418, 1026, 696. MP: >300 °C.

Electrochemical experiments

A computer-controlled potentiostat (model: CHI620C, CHI Instruments) was used to carry out electrochemical tests such as cyclic voltammetry and differential pulse voltammetry. DCM solvent was used for the 1 mM concentration solutions, and a 0.1 M concentration of tetrabutylammonium perchlorate (TBAP) was used as the supporting electrolyte. In the experiments, a calomel electrode (SCE) served as the standard electrode, a glassy carbon electrode was used as the working electrode, and platinum wire functioned as the auxiliary electrode.

Computational details

Density functional theory (DFT) and time-dependent density functional theory (TD-DFT) were implemented for optimization and absorption properties using the Gaussian 16 W quantum chemical software.[25] Frontier molecular orbitals, major transitions, percentage weight contributions, HOMO and LUMO energies, the HOMO–LUMO gap and emission energies are calculated using the same level of theory.

UV-visible absorption and steady-state photoluminescence (PL)

The UV-visible absorption spectra of the samples were measured using a commercial UV-visible spectrometer. We used DCM solvent to prepare the solution sample at a concentration of 0.1 mM. The PL was measured using an FLS 1000 fluorescence spectrometer (Edinburgh Instruments Ltd). To study the time-resolved photoluminescence (TRPL), a picosecond pulsed diode laser of 640 nm wavelength was used. The time-correlated single-photon counting (TCSPC) technique was employed to measure the TRPL. An instrument response function (IRF) was obtained using a diluted Ludox solution. The TRPL curves were fitted using bi-exponential fitting parameters and the deconvolution approach. The quality of the fits was assessed *via* residual calculations ($\chi^{(2)}$).

Femtosecond transient absorption spectroscopy (fs-TAS)

We used a HELIOS pump–probe spectrometer called (Ultrafast Systems) to carry out the femtosecond TAS. A LIBRA Ti:sapphire amplifier was used as the laser source, which generated 1 kHz, 4 mJ pulses with an 800 nm central wavelength and a pulse duration of approximately 70 fs. The source pulses were split into two beams, with one beam being used to create a white-light continuum for the probe beam by passing it through a sapphire window. The other beam was doubled in frequency using a BBO crystal to create a 400 nm pump beam. A LabVIEW-based system was employed to regulate the pre-set optical delay, and the optical chopper of the HELIOS was used to halve the pump frequency to 500 Hz. The TAS measurements were performed on solutions with a concentration of 10^{-4} M using DCM solvent, which were placed in a 1 mm path-length quartz cuvette. A kHz scan rate multichannel fiber-coupled detector was used to collect the transient signal, and the Surface Xplorer program was used to obtain the data. The collected data were analyzed using global and target analysis methods to build a photophysical model that incorporates various rate constants related to the spectra of the specific species.[26,27]

Femtosecond Z-scan experiments

In the Z-scan experiments, a standard setup[27–31] was used with the Ti:sapphire laser amplifier (LIBRA) as the light source, emitting at a 800 nm central wavelength, with a 70 fs pulse duration, and a 1 kHz repetition rate. The estimated peak intensity was about 180 GW cm^{-2}. Samples of 0.1 mM concentration were placed in a 1 mm path-length quartz cuvette, which was moved on the Z-axis using a motorized stage. The signal transmitted through the samples was detected using a silicon photodiode (PD; Thorlabs). To perform closed aperture (CA) Z-scan experiments, the transmitted signal was made sensitive to the center area of the beam by closing the aperture at the far-field site before the photodiode. The Z-scan data had a maximum estimated error of ~7% owing to input laser fluctuations, stage backlash, and error in the peak intensity estimation. The input peak intensity was optimized to minimize the effects of the pure solvent, which was validated by measuring the Z-scan of the pure solvent (maintaining the same experimental conditions), which exhibited an insignificant NLO transmittance.

Results and discussion

The synthetic route for synthesizing all three novel phthalocyanines is demonstrated in Fig. 2. The intermediate **ThIm** was synthesized by refluxing benzil, 5-formyl-2-thiopheneboronic acid and *p*-anisidine in acetic acid. The phthalonitrile **TIPn** was synthesized *via* the Suzuki coupling reaction between **ThIm** and 4-iodophthalonitrile using Pd as a catalyst. Finally, the free-base phthalocyanine (H$_2$-TIPc) was synthesized using the Li and pentanol method, and corresponding Cu(II) and Zn(II) insertion was carried out using the respective metal acetate. All three phthalocyanines and intermediates are soluble in various organic solvents, which enabled us to characterize them *via* various spectroscopic techniques, including ^{1}H NMR, elemental analysis, MALDI-MS and IR. The elemental analyses of the three phthalocyanine derivatives were found to be as predicted (see Experimental details section). The presence of molecular ion peaks in the MALDI-TOF-MS confirms that the novel Pc derivatives maintained their molecular integrity.

Absorption and photoluminescence studies

The normalized UV-visible absorption and fluorescence spectra of the Pc samples in DCM solvent are illustrated in Fig. 3(a). The absorption spectra of both the free-base and metallated Pc molecules were observed to be broad, from the UV to the visible region. The absorption and photoluminescence (PL) maxima are listed in Table 1. The absorption spectra showed a Soret band (or B-band) absorption around 360 nm due to a strong electronic transition from deeper π-levels to the LUMO level and an imidazole group absorption caused by π–π* transitions. In addition, the band covering 600–750 nm is known as the Q-band of phthalocyanine and is formed due to π–π* transitions
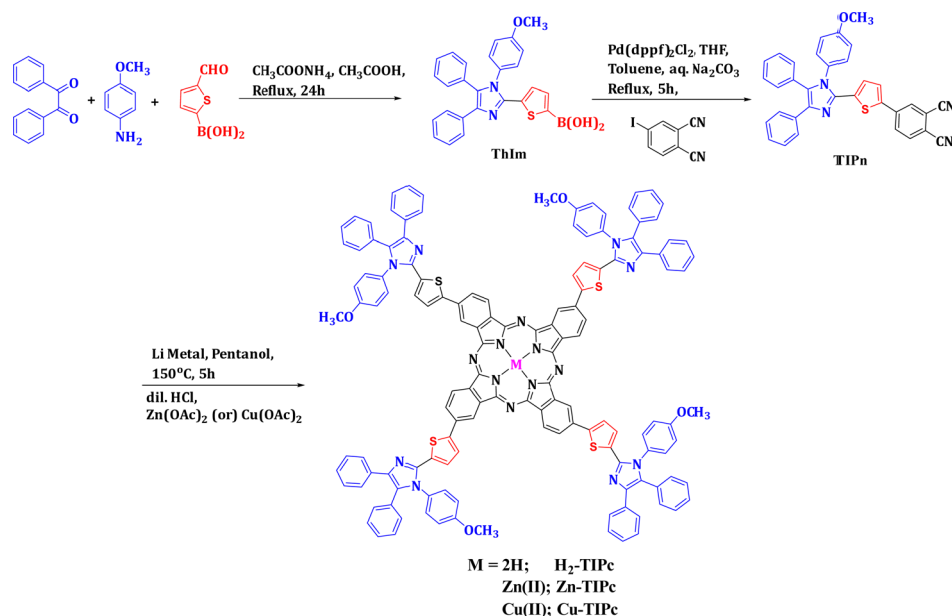
Fig. 2 Synthetic scheme of the novel phthalocyanines investigated in the present study.
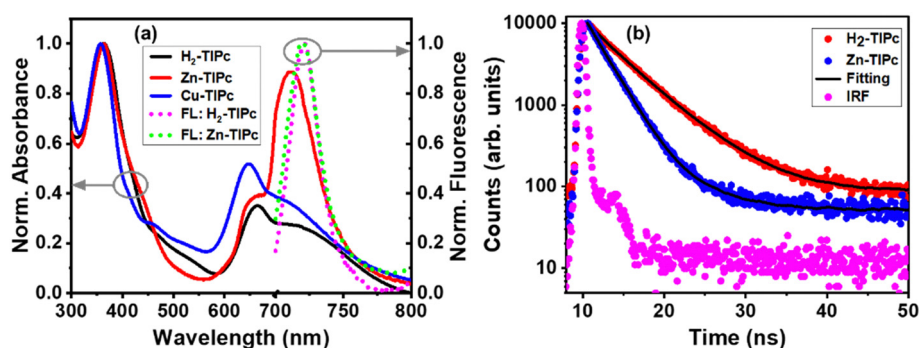

Fig. 3 (a) Normalized UV-visible absorption spectra of the Pc molecules and normalized fluorescence spectra of H$_2$-TIPc and Zn-TIPc; and (b) TRPL curves at the emission wavelength of 730 nm measured *via* TCSPC. The experimental data are represented by the scattered points, while the fitting is depicted the solid black lines.

Table 1 Data from the absorption, PL and redox properties

| Sample | UV-visible absorption maximum | | PL | Redox properties | |
	Soret band maximum (nm)	Q-band maximum (nm)	At 660 nm excitation	E_{ox} (V)	E_{red} (V)
H$_2$-TIPc	360	664, 712	721	0.85, 1.25	−1.15
Zn-TIPc	361	655, 710	720	0.77, 1.13, 1.74	−0.96
Cu-TIPc	356	646, 707	—	0.77, 0.92, 1.15	−0.97

(HOMO–LUMO transition) of the phthalocyanine moieties. Cu-TIPc exhibited a slightly smaller blueshift compared with Zn-TIPc, indicating that the Cu metallated Pc derivative possessed a lower-lying ground-state energy level. The phthalocyanine core's metal binding caused the metallo derivatives to exhibit a blueshift in the Q-band region, suggesting that the vibronic states remained stable. This is in contrast to the free-base Pc. The aggregation behavior of these Pc systems was studied by modifying the concentration in DCM solvent within the Beer–Lambert law limits. Aggregation occurs *via* coplanar interaction, resulting in monomer conversion to higher-order

complexes and less solubility in many organic solvents. This behavior is influenced by various factors such as the concentration, temperature, substitution type, metal ions, and solvent polarity.[32] The Q-band absorption intensity was found to increase linearly with increasing Pc concentration, indicating that no aggregated species existed. As a result, it was concluded that the phthalocyanines were monomeric at various concentrations, and no new blueshifted band was identified due to aggregation, as shown in Fig. S1 in the ESI.†

The fluorescence spectra of the samples were obtained using an excitation wavelength of 660 nm. The highest photoluminescence

(PL) peak for H2-TIPc was observed at 721 nm and for Zn-TIPc at 720 nm, as shown in Fig. 3(a). However, due to the paramagnetic nature of the Cu substituent, there was a very much lower emission observed from Cu-TIPc, and its PL spectra were undetectable. The PL bands of both H2-TIPc and Zn-TIPc showed no significant Stokes shifts, and they coincide with the Q-band of Pc absorption. This overlap can increase the resonance energy transmission within the monomer through Förster resonance energy transfer (FRET).[23] FRET involves an excited chemical group (the donor, D*) transferring energy to an electron on the acceptor (A) in the ground state and exciting it, causing it to return to the ground state. This can be expressed as D* + A → D + A*. FRET can modify the photoactivity of a photosensitizer. The fluorescence quantum yield was reduced due to the competing FRET process, which enables nonradiative intramolecular energy transfer within the molecule.

The lifetimes of the phthalocyanines are directly impacted by all of these properties. Using the TCSPC approach with a pulsed excitation of 640 nm, lifetime analysis of the H_2-TIPc and Zn-TIPc molecules was performed for the emission wavelength of 720 nm [Fig. 3(b)]. For H_2-TIPc and Zn-TIPc, the TCSPC data were best fitted bi-exponentially, with dominant lifetime components of 4.97 and 2.30 ns, respectively. The TRPL data indicated that the lifetime of the metallated derivative was shorter compared with that of the free-base phthalocyanine. Table S1 in the ESI† includes a list of the lifetime values. From the photophysical characteristics, it is clear that Pc systems exhibit UV-to-visible absorptions and fast lifetime-decay phenomena.

Electrochemical and spectroelectrochemical properties

We adopted both the cyclic voltammetry (CV) and differential pulse voltammetry (DPV)[33] techniques in order to estimate the redox potentials of the newly synthesized phthalocyanines. In its usual oxidized state, phthalocyanine is an aromatic system comprising 18 π-electrons and two negative charges. However, it can lose either one or two electrons when it undergoes oxidation, and, on the other hand, it can gain between one to four electrons when it undergoes reduction. The electron density of a molecule may vary due to the presence of electron-donating or electron-withdrawing substituents, resulting in changes in the positions of the HOMO and LUMO levels. Fig. S2(a)–(c) in the ESI† present the cyclic voltammograms of all the investigated phthalocyanines in 0.1 M tetrabutylammonium perchlorate (TBAP) DCM solution.

The DPV curves are shown in Fig. S2(d)–(f), ESI.† Each phthalocyanine undergoes one reversible reduction: at −1.15 V vs. SCE in the case of H_2-TIPc, whereas, in the case of the metallo derivatives, the reduction is cathodically shifted and appears at −0.97 and −0.96 V vs. SCE for Cu-TIPc and Zn-TIPc, respectively. By contrast, it was observed that each phthalocyanine undergoes either two or three quasi-reversible oxidations under the experimental conditions. The redox potentials (E_{red}) and oxidation potentials (E_{ox}) are presented in Table 1. The addition of four thiophene groups that donate electrons to each phthalocyanine ring may make the process of oxidation easier, leading to a reduction in the oxidation potential.[34] Phthalocyanines generally have a well-known electrochemical performance, and the redox properties of these Pc molecules are ascribed to the phthalocyanine ring-based electron-transfer process.[18] The nature of the redox properties can be validated via spectroelectrochemical experiments.

Spectroelectrochemical[35] investigations were carried out to examine the changes that occurred during the redox reactions of these novel phthalocyanines. Fig. 4(a) and (b) illustrate the
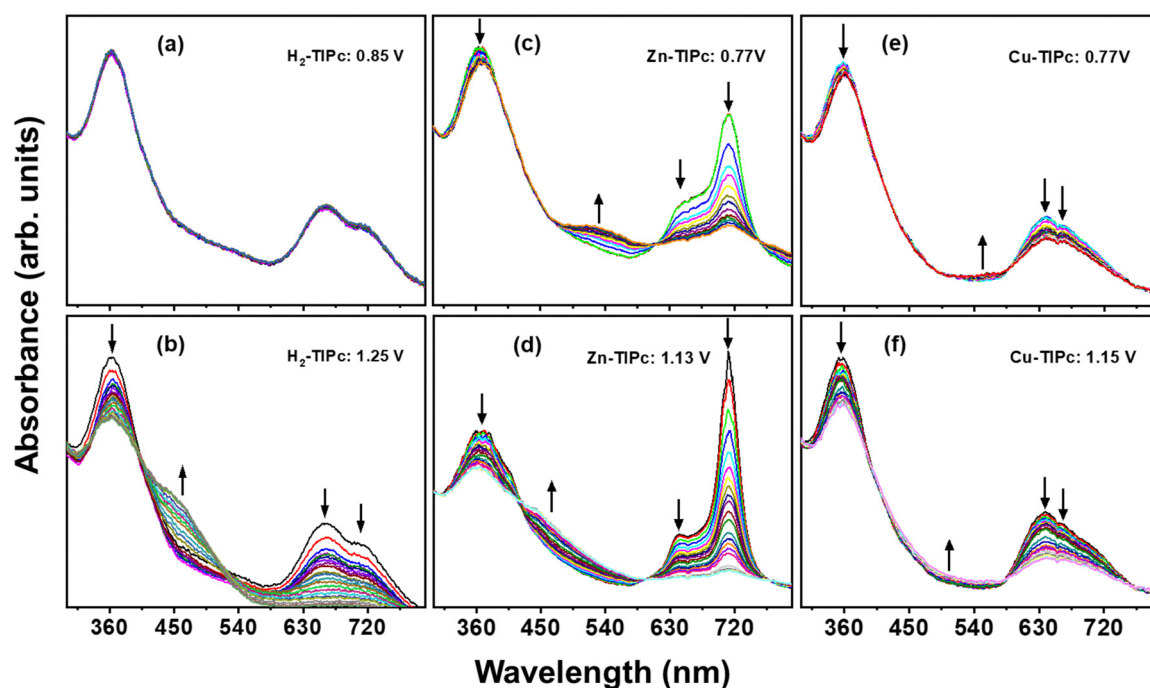

Fig. 4 *In situ* UV-visible spectroelectrochemical changes of H_2-TIPc (a) and (b), Zn-TIPc (c) and (d) and Cu-TIPc (e) and (f).

spectral changes of H_2-TIPc under different applied potentials. It is known that adjusting the strength of the Q band without shifting and observing additional bands are typical features for Pc-based electron-transfer processes.[36]

During the controlled potential oxidation of H_2-TIPc at an applied potential of 1.25 V, the intensity of the Q bands at 660 and 710 nm is reduced without forming any new band. By contrast, the intensity of the Soret band at 360 nm decreases while a shoulder emerges at 465 nm. As this occurs, isosbestic points become apparent at 400 and 520 nm, indicating that oxidation results in a single product. Furthermore, the isosbestic points demonstrate the chemical reversibility of the electron transfer reactions. The oxidation process that takes place here is ring-centered. Similar spectral changes were observed in the metallo derivatives. Due to the redox inactivity of the Zn^{2+} and Cu^{2+} metal cores[36] of Zn-TIPc and Cu-TIPc, respectively, all redox features are attributed to the Pc ring. The spectral changes that occurred during the oxidation process for Zn-TIPc and Cu-TIPc at the specified applied potential are demonstrated in Fig. 4(c)–(f). The changes in the absorption spectra at an applied voltage of 0.77 V [Fig. 4(c) and (e)] were attributed to oxidation species from $[Zn^{II}Pc^{2-}]^{1+}$ to $[Zn^{II}Pc^{1-}]^{1+}$ for Zn-TIPc and from $[Cu^{II}Pc^{2-}]^{1+}$ to $[Cu^{II}Pc^{1-}]^{1+}$ for Cu-TIPc. Fig. 4(d) and (f) depict the changes in the spectra during the oxidation process at a potential of 1.13 V for Zn-TIPc and 1.15 V for Cu-TIPc, which support the further oxidation from $[Zn^{II}Pc^{1-}]^{1+}$ to $[Zn^{II}Pc^{0}]^{2+}$ for Zn-TIPc and from $[Cu^{II}Pc^{1-}]^{1+}$ to $[Cu^{II}Pc^{0}]^{2+}$ for Cu-TIPc. During the reactions, a decrease in the intensity of the bands occurs due to decomposition of the electrogenerated cationic species. As with free-base Pc, the isosbestic points were observed clearly for these metallated Pcs, suggested the chemical reversibility of the electron transfer reactions.

Theoretical studies

Geometry optimization. All the molecules studied here were optimized *via* DFT and TD-DFT in the ground and the first excited states using a mixed basis set, respectively. The hybrid functional B3LYP with the 6-31G(d,p) basis set was used for the non-metallic part, and for the metallic parts (Cu, Zn) the LANL2DZ basis set was used. The zero negative frequencies confirm the stability of the molecules on the potential energy surface diagram. The optimized structures of these newly synthesized molecules in the ground state and the first excited state are given in Table S2 (ESI†), which comprises the phthalocyanine macrocycle, thiophene and triphenylimidazole moieties.

UV-visible absorption and emission studies. To understand the absorption properties, TD-DFT calculations are performed on the fully optimized geometries in ground state (S_0) of the reported molecules using the TD-B3LYP/6-31G(d,p) level of theory. TD-DFT calculations were performed on the first excited state (S_1) optimized geometries at the same level of theory to reveal the emission energies. In Table 2, the TD-DFT derived absorption energies, the oscillator strength (f), main transitions (MTs), percentage contribution (%Ci) > 10 and emission energies are listed. The absorption maxima for H_2-TIPc, Zn-TIPc and Cu-TIPc are 716 nm, 703 nm and 701 nm, respectively,

Table 2 TD-DFT-derived absorption energies (λ_{abs}, in nm), oscillator strength (f), main transitions (MTs) and percentage contribution (% Ci) > 10 at the TD-B3LYP/6-31G(d,p) level in combination with LANL2DZ

Molecule	λ_{abs} (nm)	f	MTs	% Ci	λ_{em} (nm) (f)[a]
H_2-TIPc	716	1.035	H → L	94	788 (1.197)
Zn-TIPc	703	0.986	H → L	94	762 (1.121)
Cu-TIPc	701	0.958	H(α) → L(α)	46	767 (1.031)
			H(β) → L(β)	48	

[a] Emission energies (λ_{em}) were calculated using TD-DFT at the TD-B3LYP/6-31G(d,p) level in association with LANL2DZ.

showing good oscillator strength. The major transitions for Zn-TIPc and Cu-TIPc are from HOMO → LUMO with a percentage weight contribution of 94. As Cu complexes always exist in doublets, therefore, the major transitions in Cu-TIPc are HOMO(α) → LUMO(α) and HOMO(β) → LUMO(β) with % weight contributions of 46 and 48, respectively.

Frontier molecular orbitals. The B3LYP/6-31G(d,p) level was utilized to approximate the frontier molecular orbitals (FMOs) (Fig. 5). The frontier molecular orbital gap contributes to characterizing the molecule's chemical reactivity and kinetic stability. It was found that the energy levels and the electron density distributions for these three phthalocyanines were relatively similar. H_2-TIPc exhibited the highest molecular orbital of −4.62 eV and a lowest unoccupied molecular orbital of −2.69 eV. Zn-TIPc showed the HOMO at −4.69 eV and the LUMO at −2.62 eV. By contrast, Cu-TIPc showed the HOMO at −4.59 eV and the LUMO at −2.62 eV. All Pcs had band gap of around 1.93–2.07 eV. Furthermore, the energy distribution and its HOMO−1 and LUMO+1 levels are shown in Fig. S3, ESI.† Therefore, it is evident that the HOMO electron distribution is present on the donor imidazole as well as on the phthalocyanine macrocycle in all three phthalocyanines, while the LUMO electron density is distributed on the phthalocyanines. From the electrostatic surface potential (ESP) diagrams, this phenomenon can be understood more clearly. The ESP describes the net electrostatic effect created in the molecule's surroundings by the overall charge distribution (electron + proton). This also helps in understanding the relative polarity of the molecule. The surface electrostatic potential is displayed using various colors on the ESP map (Fig. S4, ESI†), where each color represents a different value: yellowish red areas represent more electron cloud or the regions with the most negative electrostatic potential; the blue color denotes less electron cloud or the regions with the most positive electrostatic potential; and green indicates regions with a very small or no potential. The green regions give information about the intermolecular interactions.[37]

Femtosecond transient absorption spectroscopy (fs-TAS) studies

Using femtosecond transient absorption spectroscopy (fs-TAS), we studied the behavior of the photogenerated carriers in the phthalocyanine samples. The aim was to understand the charge-transport properties of the samples and their relationship with the metal substitutions. A white-continuum covering a wavelength range of 430–780 nm was used to investigate the first 5 ns following excitation of the samples using a 400 nm
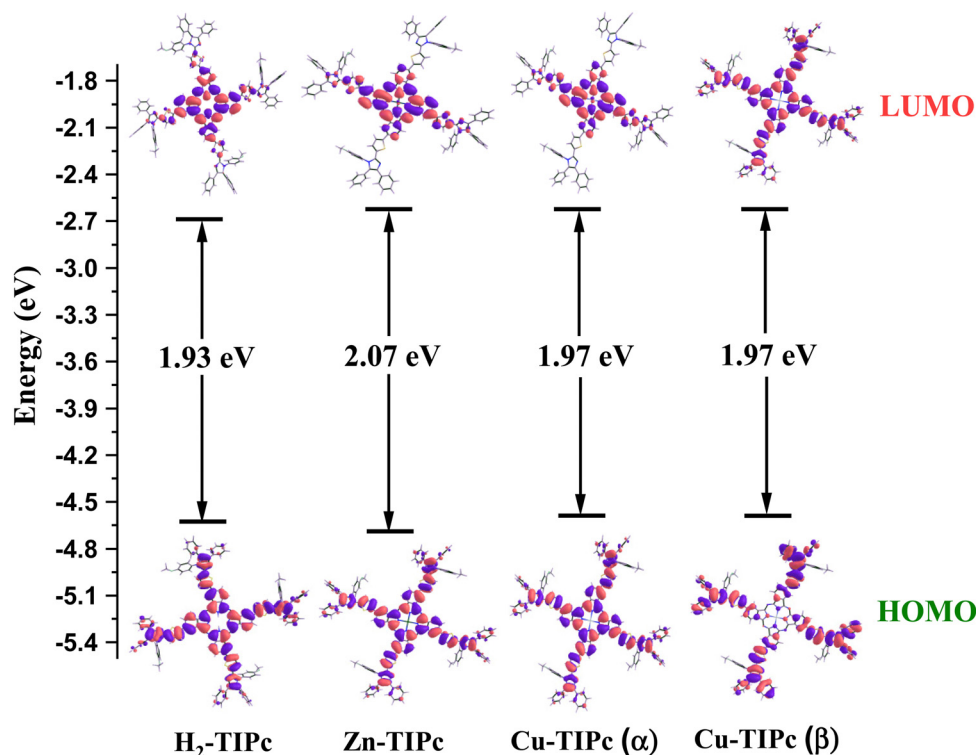
Fig. 5 Isodensity plots of the frontier molecular orbitals (FMOs) based on the B3LYP/6-31G(d,p) method and energy level diagrams.

pump beam. We measured the absorption difference [ΔA (mOD)] signals from fs-TAS. Fig. 6 and Fig. S5, ESI† show the evolution of the TAS intensity profile for these three Pcs in detail with an increasing delay time between the pump and probe pulse. A positive band indicates a decrease in absorption, whereas a negative band indicates an increase in absorption. The ground-state bleach band (GSB$_{Q\text{-band}}$) or photobleach (PB) band from S_0 to higher excited states causes the TAS to exhibit negative differential absorption characteristics in the Q-band wavelength regions. Following the process of photoexcitation, the ground state experiences a reduction in population leading to the generation of the ground-state bleach (GSB) band. The appearance of the GSB$_{Q\text{-band}}$ is also associated with the overlaps between the PB band and the stimulated emission (SE) band, which is caused by the photoluminescence (PL) of the molecules in the same part of the spectrum. We could not observe the GSB corresponding to the B-bands due to the limitation of our probe wavelength range. Typically, a large positive difference in absorption is associated with singlet and triplet excited-state absorption (ESA).[27] This absorption occurs because the population is absorbed into locally excited (LE) states from the excited state S_1. Thus, the signal obtained from transient absorption spectroscopy (TAS) within the measured spectral range is created via the combination of excited-state absorption, stimulated emission, and ground-state bleaching.

Different TAS features of our Pc systems are shown in Fig. 6(a)–(c) and Fig. S5(a)–(c), ESI.† The ESA bands or photoinduced absorption (PIA) bands were observed in the spectral range of 430–625 nm, 430–620 nm and 430–615 nm for H$_2$-TIPc, Zn-TIPc, and Cu-TIPc, respectively. The GSB$_{Q\text{-band}}$ spanned the

wavelength range of 625–748 nm, 620–745 nm and 615–685 nm, respectively for H$_2$-TIPc, Zn-TIPc, and Cu-TIPc. Another PIA band was observed after 748 nm to longer wavelengths for H$_2$-TIPc, from 745 nm to a longer spectral range for Zn-TIPc, and after 685 nm to longer wavelengths for Cu-TIPc. It was observed that the positive ESA maxima for these Pc samples were very long-lived (typically >1 ns). The ESA did not decay completely until at least 5 ns for the metallated Pcs. This denotes the presence of a triplet state in these compounds.[18] Due to the loss of excited state absorption, we noticed the bleach signal, which showed a longer decay. The strong PIA signals and the strong photobleach signals for the metallated Pcs indicate the yield of triplets to be higher. For Cu-TIPc, we see the formation of the GSB$_{Q\text{-band}}$ close to 645 nm from 300 fs to 5 ns. The evolution of the GSB$_{Q\text{-band}}$ is attributed to the increase in the population of the S_1 state and the decline of the competing ESA band. The metallated Pcs displayed a blueshift in their ESA bands with decreasing intensities within the 300 fs to 5 ns delay time range. This shift towards shorter wavelengths is probably due to the involvement of higher excited states in forming the ESA bands over time. The spectral shape of the PIA and PB bands remained relatively constant from shorter to longer time delays, indicating that they originated from the same excited species. The H$_2$-TIPc sample displays faster decay than the metallated Pcs and an almost complete decay of the ESA and PB bands, reaching the 5 ns delay time [Fig. 6(a) and Fig. S5(a), ESI†]. However, Cu-TIPc shows dissimilar decay phenomena compared with the Zn-based counterpart; the PB signal of Cu-TIPc increases within the 5 ns time frame.
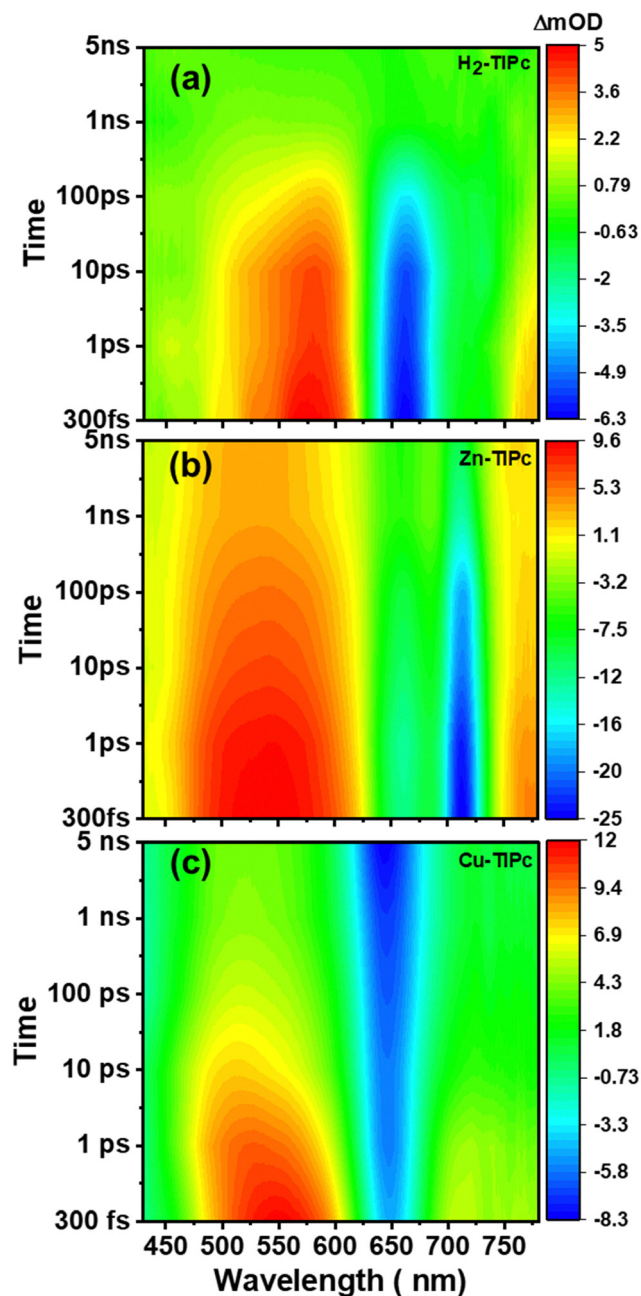
Fig. 6 Pseudo-colour plots of the fs-TAS data collected with Soret band photoexcitation for solutions of (a) H_2-TIPc, (b) Zn-TIPc and (c) Cu-TIPc.

When we fitted the TAS data with a single wavelength-kinetic trace, it was hard to grasp the dynamics of the excited carriers or evaluate the decay rate constants because multiple spectra form and different excited-state processes change over time and overlap. Therefore, the global and the compartmental target analysis models[38] were considered to understand the TAS data matrix in detail. We used Glotaran software[39] for the global and target analysis and obtained the evolution-associated decay spectra (EADS) and species-associated difference spectra (SADS), respectively. The time constants of various excited states acquired from the global model analysis were used to

generate the SADS. The parallel and sequential models were combined in the compartmental or target analysis model. The compartmental model, which includes compartment decay and population transfer across compartments, accounts for all possible branching ratios with the given rate constants.[40] We focused on analyzing the relaxation pathways and explaining the specific details of these pathways within the compartmental system for the measured TAS data.

In Fig. S6, ESI,† a schematic displays the overall photophysical model of the examined Pc systems. The 400 nm pump pulse excites the systems into the locally excited states, and Kasha's rule predicts a quick relaxation to a lower excited state. The photophysical model encompasses various photoprocesses, such as internal conversion from the localized excited state (S_n) to the singlet excited (S_1), relaxation within the vibrational states of S_1, decay through radiation to the ground states (S_0) from the intermediate S_1 states, nonradiative crossing between singlet (S_1) states and triplet (T_1) states (or the tripdoublet ($^2T_1$) state for Cu-TIPc), and the relaxation of triplet states to S_0 states. Therefore, there are many intermediate states involved in these systems. Similar systems reported in some published articles[23,41] illustrated evidence of the involvement of intermediate states in the relaxation pathways. Fig. 7(a)–(c) show the SADS for H_2-TIPc, Zn-TIPc and Cu-TIPc, respectively, that were obtained from the target analysis, and Fig. 7(d)–(f) display the related population decay of different states. The black-colored SADS1 spectra are connected to the S_n states. These states have a lifetime of 303 fs for H_2-TIPc, 315 fs for Zn-TIPc and 340 fs for Cu-TIPc. The hot S_1 states are responsible for the SADS2 spectra (red), where τ_2 = 18 ps, 20 ps, and 11 ps are the lifetimes of the hot S_1 states of H_2-TIPc, Zn-TIPc and Cu-TIPc, respectively. The SADS3 spectra (blue) and the respective lifetimes τ_3 = 0.43 ns, 0.61 ns, and 1.21 ns for H_2-TIPc, Zn-TIPc and Cu-TIPc are of the S_1 states. The S_1 states can undergo relaxation through two distinct pathways. The first one is the emission of radiation, which causes the population of the S_1 states to return to the S_0 state. The second pathway is referred to as intersystem crossing, where the population of S_1 states moves to triplet T_1 states (or $^2T_1$ states in the case of Cu-TIPc). Finally, the respective lifetimes of τ_4 = 0.004 μs, 4.36 μs, and 12.20 μs are for the T_1 states for H_2-TIPc, Zn-TIPc and Cu-TIPc. The SADS4 spectra (green) are attributed to the lifetimes τ_4. It is noticed that the value of τ_4 is the highest for Cu-TIPc. The reason for this is probably that Cu-TIPc showed dissimilar transient absorption spectra compared with the Zn-based Pc [Fig. 6(b) and (c)]. We also observed that the metallated Pc molecules have longer triplet lifetimes than the free-base Pc molecule. The sufficient charge flow from the metal core is the underlying cause. Furthermore, the difference in the lifetime of the metallated Pcs is attributed to the greater impact of spin–orbit coupling, which is brought about by the presence of the Cu or Zn atom. Compared with its Zn-based counterpart, Cu-TIPc demonstrated longer relaxation kinetics. The reason for this is the incomplete filling of d-orbitals and the electronic configuration ($3d^9\ 4s^2$) of copper (atomic number 29). This leads to a higher possibility of interactions between the
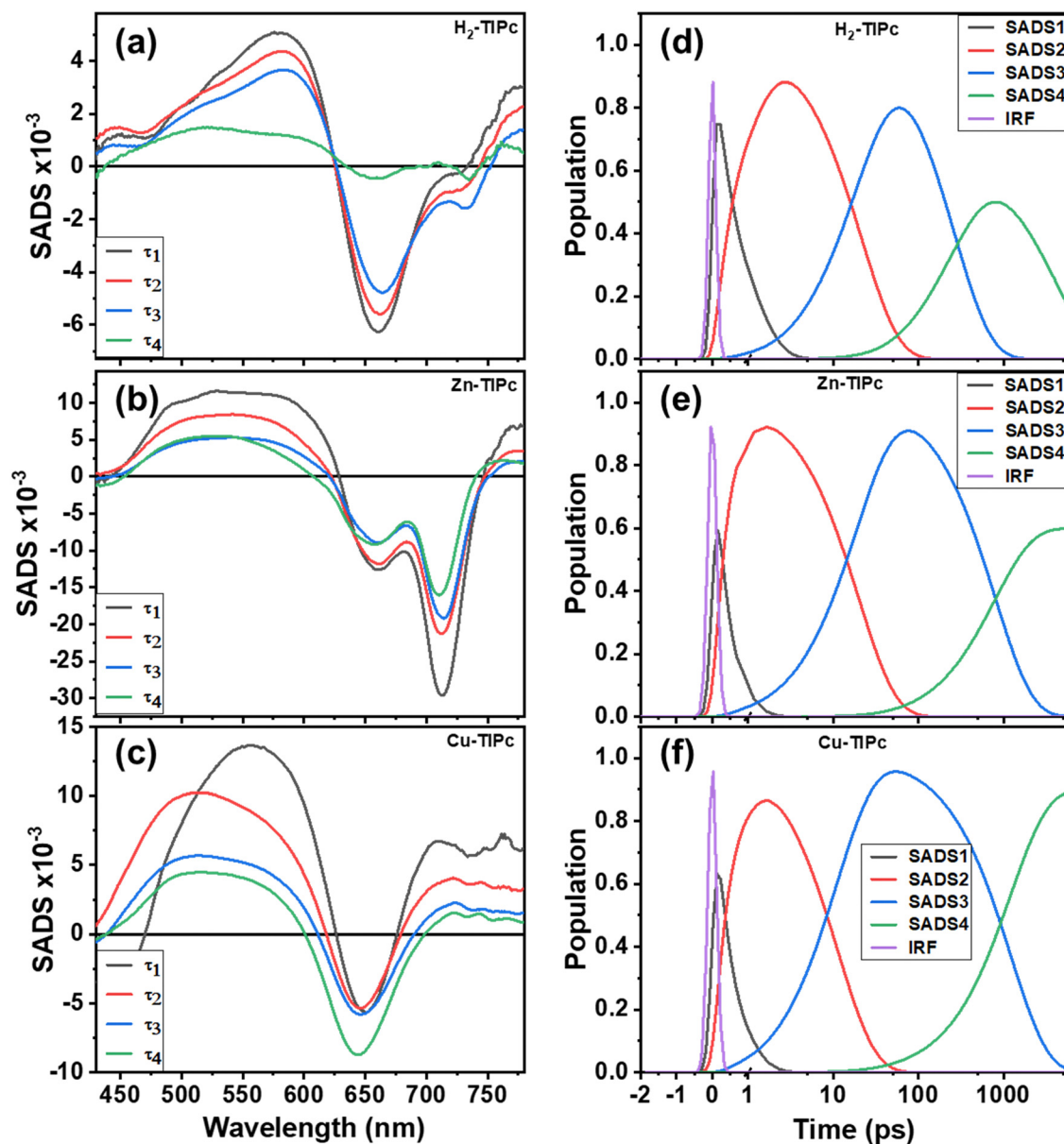
Fig. 7 Species associated difference spectra (SADS) obtained from the target analysis of TAS data for (a) H_2-TIPc, (b) Zn-TIPc and (c) Cu-TIPc; and population decay profiles of the respective SADS for (d) H_2-TIPc, (e) Zn-TIPc and (f) Cu-TIPc.

central copper metal and peripheral groups, compared with zinc (atomic number 30), which has a filled d-orbital with an electronic configuration of $3d^{10}4s^2$, and hence fewer donor–acceptor interactions. As Cu(II) has an unfilled d-orbital, the Cu-based Pc derivative should have the doublet state. Moreover, the presence of the doublet in Cu-TIPc is proved from the DFT calculations. Thus, the triplet state of Cu-TIPc is called a tripdoublet $(^2T_1)$.[41–44] This indicates that the ISC process between the Zn-based and Cu-based Pcs is different.

The PB band signal of the corresponding Zn-TIPc at the maximum point [PB band in Fig. 6(b)] shows a continuous decay; Cu-TIPc shows no decay within a few nanoseconds [PB band in Fig. 6(c)] unlike Zn-TIPc. Because there is no observable fluorescence for Cu-based Pc in this higher wavelength area, no

stimulated emission is predicted in this system. The divergence of the Cu-TIPc decay curves can be attributed to the enhancement of molecular interaction and the acceleration of excitation coupling through the Förster energy transfer process. This process facilitates the transfer of energy between closed molecules through $\pi–\pi^*$ transitions,[44] leading to improved efficiency in the system. These factors are the most probable reasons behind the observed divergence of the decay curves. The signal in a phthalocyanine should ultimately decrease to zero over a longer time due to the energy relaxation process. The strong GSB of Cu-TIPc develops into a lengthy process and does not complete its decay within our detection frame (5.0 ns). It eventually decays to the zero level over a longer timeframe.

Table 3 Summary of the rate constants and lifetimes of different states obtained from the target model analysis of TAS data

Sample	Rate constants					Lifetimes			
	k_{12} (fs)$^{-1}$	k_{23} (ps)$^{-1}$	k_{30} (ns)$^{-1}$	k_{34} (ns)$^{-1}$	k_{40} (μs)$^{-1}$	τ_1 (fs)	τ_2 (ps)	τ_3 (ns)	τ_4 (μs)
H$_2$-TIPc	303	18	4.30	0.47	0.004	303	18	0.43	0.004
Zn-TIPc	315	20	2.77	0.78	4.36	315	20	0.61	4.36
Cu-TIPc	340	11	60.5	1.23	12	340	11	1.21	12.2

Fig. 7(d)–(f) shows the depopulations of the four excited states. In all of the molecules, the relaxation of SADS1 takes place through a single channel whereby the population decays from the S_n to S_1 states at a rate constant of $k_{12} = \tau_1^{-1}$. SADS2 experiences a nonradiative pathway with a rate constant of $k_{23} = \tau_2^{-1}$, where the population decays from the hot S_1 state to the thermally relaxed S_1 state. Afterward, there are two channels by which SADS3 depopulates: a radiative decay from the S_1 to S_0 states with a rate constant of k_{30}, and a nonradiative process from S_1 to T_1 or the $^2T_1$ states, *i.e.*, an ISC process with a rate constant of k_{34}. The relationship between k_{30} and k_{34} is described by $k_{30}k_{34} = \tau_3^{-1}$. The proportion of the population that experiences radiative decay and the ISC process varies for each of the three Pc systems, as shown by the fluorescence quantum yields. Finally, the tripdoublet or triplet state of SADS4 decays steadily to S_0 states with a rate constant of $k_{40} = \tau_4^{-1}$.

Table 3 lists the lifetimes and microscopic rate constants of various intermediate states of the examined Pc molecules. Fig. 8(a)–(c), shows two TAS spectra with delay times of 1 ps and 2 ns, and Fig. 8(d)–(f), displays kinetic traces acquired at wavelengths of 560 and 660 nm that represent several bands, including PIA, GSB, and SE. These figures show the accuracy of our target analysis model for H$_2$-TIPc, Zn-TIPc and Cu-TIPc. The results of the target analysis were used to fit (black lines) the experimental data. The black lines serve as a confirmation of the accuracy of the photophysical model since they overlap well with the experimental data points.

Now, we discuss implementing the longer decay times for metallated Pcs investigated here from the aspect of device applications. Compared with Zn, the Cu element has different intermediate decay states and increased tripdoublet lifetime. The characteristics of the triplet state and the transportation of electrons and holes can be impacted by core metals and asymmetrical metallated Pcs. It seems that the possibility of enhancing the diffusion length (L_D) through the triplet sensitization pathway is supported by the fact that triplet-state excitons have a longer decay time.[44] Longer L_D can enhance the charge transportability by limiting carrier recombination in the transporting layer, resulting in improved efficiency. Therefore, since the long decay of triplet (or tripdoublet) states is advantageous for the movement and extraction of electric charge, metallated Pcs are a promising option as a transport layer to enhance the effectiveness of a device. Future work will be required to understand this point in more detail by obtaining diffusion coefficient (D_E), hole mobility and L_D in a device based on these metallated Pcs.

Femtosecond Z-scan toward NLO applications

The photoactivity prospects for the phthalocyanine samples with excitation at 400 nm were validated through the transient absorption measurements. To realize the application of the metallated phthalocyanines as a potential nonlinear optical material, the fs Z-scan experiments were carried out using 800 nm non-resonant excitation. These donor–acceptor compounds are estimated to have high NLO parameters, not only because of the extended π-electron delocalization of the Pc ring system but also due to the asymmetrical electronic structure generated from the ring substitution. The multiphoton absorption properties of these molecules were investigated using open-aperture (OA) Z-scan experiments, whereas the nonlinear refractive index, second hyperpolarizability and third-order nonlinear susceptibility were accessed using closed-aperture (CA) Z-scan experiments.

The symmetric transmission plots of the OA Z-scan curves are shown in Fig. 9(a)–(c). As the intensity of the incident laser beam increases closer to $Z = 0$, the transmittance intensity through the sample is reduced until it saturates with the incident intensity. Each sample possesses reverse saturable absorption (RSA) characteristics. If the ESA contribution is larger compared with the ground-state absorption, the sample exhibits strong RSA behaviour. When the cross-section of the singlet-to-singlet (S_1–S_2) or triplet-to-triplet (T_1–T_2) transitions is greater than that of the ground state, reverse saturation occurs.[45] While RSA can show small absorption at low incident laser intensities, it can also show significant absorptions through the nonlinear absorber at high incident laser intensities.

At 800 nm excitation, we found minimal one-photon absorption for all of these compounds [Fig. 3(a)]. Importantly, the conditions of our experiments prevent the direct transition of an electron from the ground state to the excited state through one-photon absorption. Thus, only multiphoton absorption can lead the electrons to an excited state. One can expect nonlinear absorption processes such as two-photon absorption (2PA) or three-photon absorption (3PA). A three-level energy model[46] for these Pc systems interacting with the ultrashort laser has been taken into account in our calculations to fully explain the nonlinear behaviour using theoretical modeling. According to analysis of the target modeling of fs-TAS results, the transition to the first triplet excited state from the first singlet excited state occurs more slowly ($\sim$ns) than the excitation laser pulse duration (70 fs). Hence, the three-level model disregards the transitions involving triplet states. The model considers all rotational and vibrational states of the first excited electronic energy state, referred to as S_1, as well as any higher excited states beyond S_1, denoted as S_n. The mechanisms related to the nonlinear absorption in these Pc molecules with electronic energy sates of S_0, S_1 and S_n are described by eqn (1)–(4). The instantaneous two-photon absorption coefficient (β) and three-photon absorption coefficient (α_3) are implemented in these coupled rate equations to achieve completeness and better
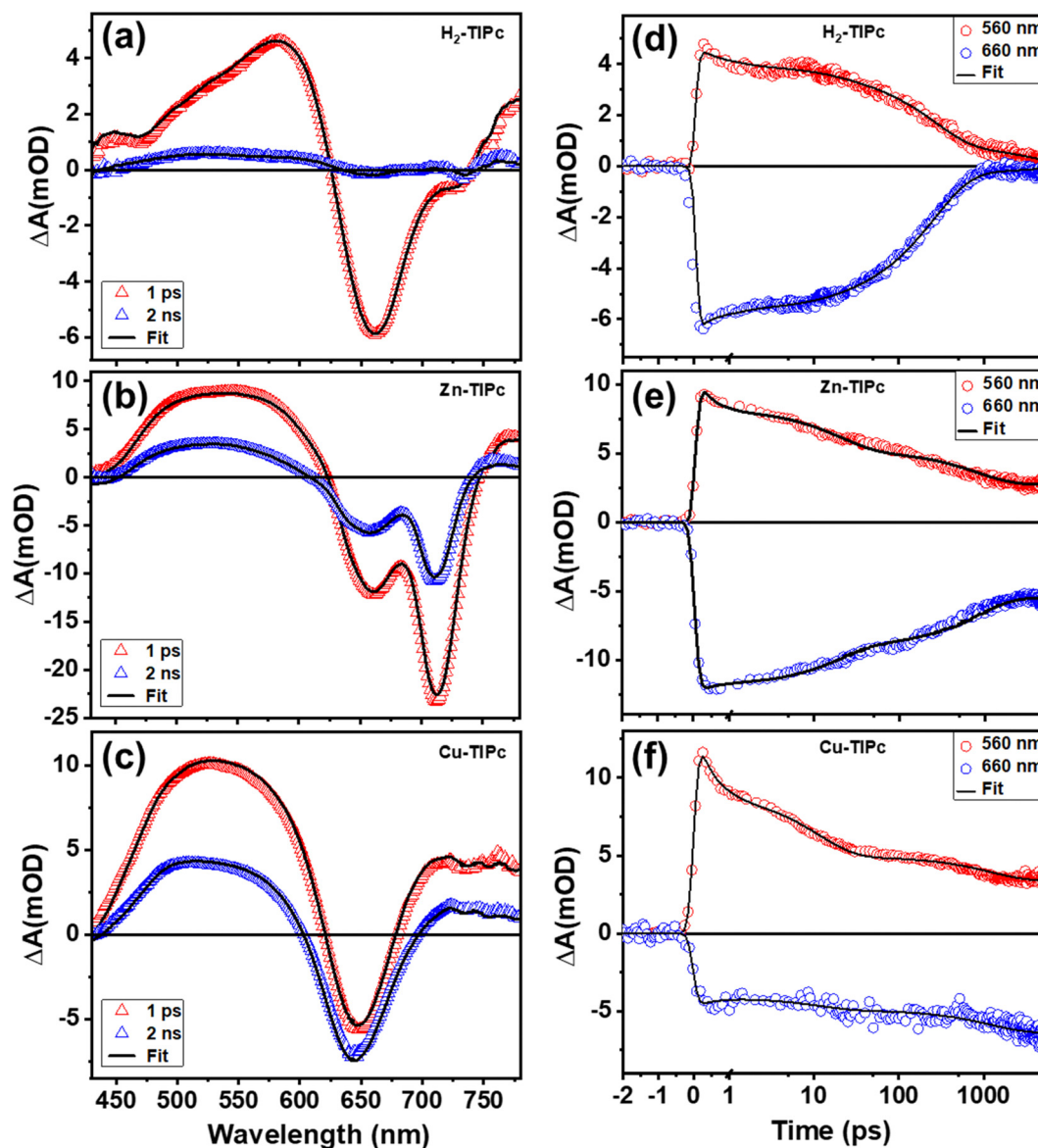
Fig. 8   (a), (b) and (c) fs-TAS at a probe delay of 1 ps and 2 ns, for H$_2$-TIPc, Zn-TIPc and Cu-TIPc, respectively; and (d), (e) and (f) TAS relaxation profiles at 560 nm and 660 nm for H$_2$-TIPc, Zn-TIPc, and Cu-TIPc, respectively. Experimental data are represented by open symbols, and the solid lines represent target analysis fittings.

fittings.

$$\frac{dN_0}{dt} = -\frac{\sigma_0 I N_0}{\hbar\omega} - \frac{\beta I^2}{2\hbar\omega} - \frac{\alpha_3 I^3}{3\hbar\omega} + \frac{N_1}{\tau_{s1}} \qquad (1)$$

$$\frac{dN_1}{dt} = \frac{\sigma_0 I N_0}{\hbar\omega} - \frac{N_1}{\tau_{s1}} + \frac{N_2}{\tau_{sn}} \qquad (2)$$

$$\frac{dN_2}{dt} = \frac{\beta I^2}{2\hbar\omega} + \frac{\alpha_3 I^3}{3\hbar\omega} - \frac{N_2}{\tau_{sn}} \qquad (3)$$

We calculated the transmission intensity through the sample using the equation:

$$\frac{dI}{dz} = -\sigma_0 I N_0 - \beta I^2 - \alpha_3 I^3, \qquad (4)$$

where $I = I_0 \times (\omega_0^2/\omega^2(z)) \times \exp\left(\frac{-t^2}{\tau_p^2}\right) \times \exp\left(-\frac{2r^2}{\omega^2(z)}\right)$, and

$\omega(z) = \omega_0\left[1 + \left(\frac{Z}{Z_0}\right)^2\right]^{1/2}$. In the above equations, N_0, N_1 and N_2 are population number densities in the states of S$_0$, S$_1$ and S$_n$, respectively, σ_0 is the ground-state absorption cross-section, $\hbar\omega$ is the energy of the incident laser beam, τ_{sn} and τ_{s1} are the lifetimes of the S$_n$ and S$_1$ states, respectively, ω_0 is the beam waist at focus, and z_0 is the Rayleigh range and τ_p represents the input pulse width. The intensity of the laser is denoted by I, which is a function of r, t and z; I_0 is the peak intensity at the focus.

To solve the coupled rate equations numerically, the Runge–Kutta fourth-order approach was used after they were decoupled
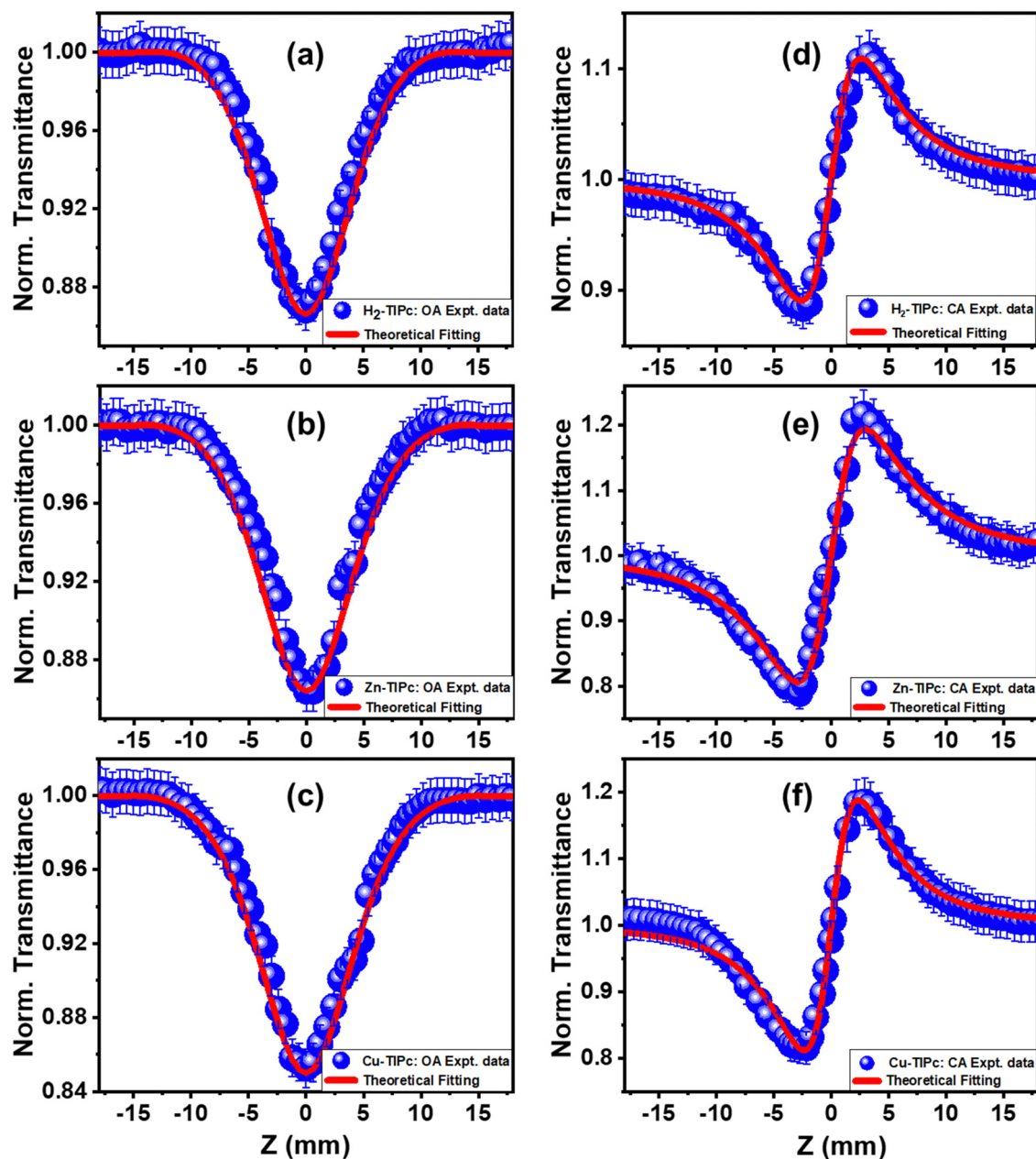
Fig. 9 (a), (b) and (c) OA Z-scan data for H₂-TIPc, Zn-TIPc and Cu-TIPc, respectively; and (c), (d) and (e) CA Z-scan data for H₂-TIPc, Zn-TIPc and Cu-TIPc, respectively. Open symbols denote the experimental data, while solid lines show the theoretical fitting.

and integrated over time (t), the radial direction (r), and z. The integration limits for t, r, and z were from $-\infty$ to ∞, 0 to ∞, and 0 to L (the sample length), respectively. The integration was carried out using 60 slices for r, 30 slices for t, and 10 slices for z. By performing a least-squares fit of the experimental OA data, we determined the values of β and α_3. The obtained values of τ_{sn} and τ_{s1} of these Pc molecules from the target analysis of the fs-TAS data (Table 3) were used as inputs for the theoretical fits. When both the 2PA and 3PA contributions[46] were accounted for in the rate equations, better fits were achieved (see Fig. S7, ESI†). The 2PA coefficient estimated for H₂-TIPc, Zn-TIPc and Cu-TIPc was 0.93×10^{-11}, 1.01×10^{-11}, and 1.40×10^{-11} cm W^{-1}, respectively.

In addition, we utilized eqn (S1) and (S2) in the ESI† to determine the values for the two-photon absorption cross-section (σ_{2PA}) and the three-photon absorption cross-section (σ_{3PA}). The nonlinear parameters that we obtained are presented in Table 4. These high 2PA cross-sections can be utilized effectively in biological imaging. Moreover, due to the higher values of the 3PA coefficient, these Pc molecules may also be used for three-photon imaging (3PI).[47] One of the most promising new advances in multiphoton microscopy technology is 3PI, which offers better spatial confinement and helps to achieve a higher contrast and resolution in imaging. 3PA-based optical limiting and three-photon pumped lasing[48] are other applications based on 3PA.

Table 4 Calculated NLO coefficients of the novel phthalocyanines from the Z-scan experiments

NLO parameter	H$_2$-TIPc	Zn-TIPc	Cu-TIPc
σ_0 (cm^2) $\times$ 10^{-18}	1.40	1.68	1.83
β (cm W^{-1}) $\times$ 10^{-11}	0.93	1.01	1.40
α_3 (cm^3 W^{-2}) $\times$ 10^{-23}	4.45	5.22	6.13
σ_{2PA} (GM) $\times$ 10^3	5.75	6.41	8.89
σ_{3PA} (cm^6 s^2) $\times$ 10^{-77}	6.81	8.23	9.65
n_2 (cm^2 W^{-1}) $\times$ 10^{-16}	3.68	6.80	5.75
$\chi^{(3)}$ (esu) $\times$ 10^{-13}	3.07	3.33	4.60
$\langle\gamma\rangle$ (esu) $\times$ 10^{-30}	2.34	2.62	3.61
DFT calculated $\langle\gamma\rangle$ (esu) $\times$ 10^{-30}	0.59	0.46	0.43
Optical limiting onset (mJ cm^{-2})	3.20	2.48	2.34
Inverse of FOM	0.67	0.43	0.59

To realize the optical limiting behavior of the examined Pcs, we calculated the optical limiting (OL) onset from the open-aperture Z-scan data.[20] A good optical limiter acts as a transparent medium at a lower incident laser fluence and as an opaque medium at a high incident laser fluence. As the input fluence increases, the transmission intensity of optical-limiting materials decreases. This process involves the intensity-dependent transmission for keeping the intensity of the transmitted light beam at a predetermined threshold. The optical limiter protects human eyes, light-sensitive optical components and optical sensors from laser-induced damage.[49] An efficient optical limiter has the following characteristics: a small optical-limiting threshold, a high linear transmittance over the sensor spectrum, stability, a high optical damage threshold, a rapid response time, and optical clarity. OL can be produced through a variety of NLO processes, such as excited-state absorption (ESA), multiphoton absorption, free carrier absorption (FCA), nonlinear scattering, photo-refraction, self-focusing, self-defocusing, etc.

In our case, we observed that multiphoton absorption leads to the OL characteristics described here. Fig. 10(a)–(c) shows the curves of the normalized transmittance of the sample verses the input laser fluence. Using the following equation,[49,50] the input laser energy was calculated based on the OA Z-scan results:

$$E(z) = \frac{4\sqrt{\ln 2}\,E_{in}}{\pi^{3/2}\omega^2(z)}. \quad (5)$$

Here, E_{in} and $\omega(z)$ represent the energy of the incident laser and the beam radius at each Z-position, respectively. The input laser fluence at which the normalized linear transmittance of the multiphoton-absorbing material deviates from linearity is known as the optical limiting onset value.[27,51] In Fig. 10, the divergence in the linearity of transmittance indicated the presence of OL in these phthalocyanine systems. The measured OL onset for H$_2$-TIPc, Zn-TIPc and Cu-TIPc is 3.20, 2.48, and 2.34 mJ cm^{-2}, respectively. The OL onset values are listed in Table 4. The examined Pc molecules have lower OL onsets, making them potentially suitable for use in optical-limiting applications. The optical-limiting onsets of these phthalocyanine molecules were found to be comparable to or better than those of compounds in earlier reports. We obtained an OL onset value of ~4 mJ cm^{-2} for the protein chromophores

uGFPc by applying an 800 nm, 70 fs laser pulses.[51] Moreover, previously, we obtained a limiting onset of 5.8 and 5.7 mJ cm^{-2} for the G1 and G3 organic dye molecules,[27] respectively, applying the same laser for excitation. In another report by us, we obtained optical-limiting onset values of 6.4 and 5 mJ cm^{-2} for the porphyrin molecules LG5 and LG6, respectively.[52] The OL behavior can also be measured via the optical-limiting threshold.

The OL threshold indicates the input laser fluence at which the normalized transmittance of the multiphoton absorbing material drops to 50%.[53] Polavarapu et al.[54] obtained the threshold values for oleylamine-capped gold nanoparticles, which were 7.5 and 0.6 J cm^{-2} using nanosecond laser pulses at 1064 nm and 532 nm, respectively. They also reported the OL threshold values of 10 and 1 J cm^{-2} for CNTs using nanosecond laser pulses at 1064 nm and 532 nm, respectively. The OL threshold for DMMC was observed by Patil et al.[49] with the value of 5.6 mJ cm^{-2} using a 150 fs laser pulse at 800 nm as the excitation source. Using a 130 fs Ti:sapphire laser pulse at 800 nm, Wei et al.[55] calculated the value of OL threshold to be 22.3 mJ cm^{-2} for the MoS$_2$/TiO$_2$ nanocomposite.

The nonlinear refractive index was obtained from the closed-aperture Z-scan data. The CA data were analyzed using eqn (S3), ESI.† From the fitted curves of CA Z-scan data, we essentially obtained the value of the on-axis nonlinear phase shift at the focus ($\Delta\Phi$). The value of n_2 for the sample varies as a result of the strong laser beam present in the system.[56] The nonlinear refractive index is related to the nonlinear on-axis phase shift[28] as follows:

$$\Delta\Phi = kI_0 n_2 L_{eff}, \quad (6)$$

where I_0 is the peak intensity of the incident laser beam, $k = 2\pi/\lambda$ is the wave vector, and L_{eff} is the effective length of the sample. For all of our investigated Pc samples, valley-peak shapes were observed for the CA data as shown in Fig. 9(d)–(f). The influence of the MPA was lessened by dividing the data of the CA Z-scan by the data of the OA Z-scan. A positive nonlinear refractive index was indicated by the self-focusing[28] behaviour of these samples. The obtained values of n_2 were 3.68 $\times$ 10^{-16}, 6.80 $\times$ 10^{-16}, and 5.75 $\times$ 10^{-16} cm^2 W^{-1}, respectively, for H$_2$-TIPc, Zn-TIPc and Cu-TIPc.

The value of the third-order nonlinear susceptibility ($\chi^{(3)}$) was calculated from the values of n_2 and β, where $\chi^{(3)}$ is a complex parameter:[57] $\chi^{(3)} = \chi_R^{(3)} + i\chi_I^{(3)}$, in which the real part ($\chi_R^{(3)}$) is related to n_2 and the imaginary part ($\chi_I^{(3)}$) is associated with the 2PA coefficient β.[58] Using the equations[18,28] shown below, we calculated $\chi^{(3)}$:

$$\chi_R^{(3)}(\text{esu}) = \frac{10^{-4}C_0^2 n_2 n_0^2\,(\text{cm}^2\,\text{W}^{-1})}{\pi} \quad (7)$$

$$\chi_I^{(3)}(\text{esu}) = \frac{10^{-2}C_0^2 \lambda\beta n_0^2\,(\text{cm}\,\text{W}^{-1})}{4\pi^2}. \quad (8)$$

In the equation above, C denotes the speed of light, ϵ_0 is the permittivity of empty space, and n_0 is the linear refractive index of the sample. As we did not know the exact values of n_0 for these samples, we took the value of the linear refractive index of DCM (solvent) to be $n_0 = 1.43$. Following eqn (S4) (ESI†),[27] we
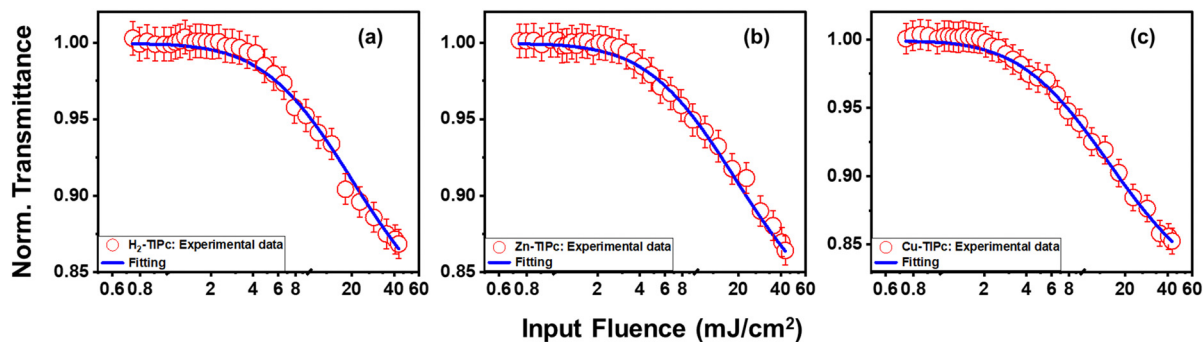
Fig. 10 Optical limiting curves of (a) H$_2$-TIPc, (b) Zn-TIPc and (c) Cu-TIPc. Open symbols denote the experimental data, while solid lines show the theoretical fitting.

next calculated the second hyperpolarizability ($\langle\gamma\rangle$) values utilizing the NLO susceptibility values. The calculated values of $\langle\gamma\rangle$ for H$_2$-TIPc, Zn-TIPc and Cu-TIPc were 2.34×10^{-30}, 2.62×10^{-30} and 3.61×10^{-30} esu, respectively. Furthermore, the DFT level is utilized to compute the second hyperpolarizability values for all of these molecules through the sum over states (SOS) approach.[59,60] The second hyperpolarizability values obtained *via* the DFT method are approximately 10^{-30} esu and are consistent with the experimental outcomes. In Table S3 (ESI†), we compare the second hyperpolarizability values that we obtained with those reported previously. The estimated values of n_2, $\chi_R^{(3)}$, and $\langle\gamma\rangle$ for each molecule are tabulated in Table 4.

We observed that the NLO coefficients obtained *via* the OA and CA Z-scan techniques are sufficiently large to indicate that these Pc systems are excellent nonlinear materials. The reason behind the improvement in the NLO characteristics may be attributed to the increased intramolecular transition dipole moment between the excited states that take part in the electronic transition while undergoing the photoinduced ET process. Moreover, the metallated phthalocyanines showed superior NLO characteristics. The metallated Pcs replaced with organic scaffolds at their peripheral locations reduce aggregation. Because the dipole moment of the axial ligand–central metal bond is perpendicular to the Pc macrocycle, axially substituted Pcs possess a weak aggregation effect and, eventually, a greater NLO response.[17]

To evaluate the strength of the NLO coefficients obtained for our molecules, we compared these values with those published in earlier reports. Previously, we obtained values of n_2 of 0.46×10^{-16} and -9.6×10^{-16} cm^2 W^{-1} for the phthalocyanines CBZPC1 and CBZPC2, respectively, applying a 50 fs laser pulse at 800 nm.[18] For another phthalocyanine, PBIPC, we obtained an n_2 value of 0.92×10^{-16} cm^2 W^{-1} and a β value of 12×10^{-11} cm W^{-1} using the same laser.[8] For another set of PCs we also calculated $\beta = 2.312 \times 10^{-12}$ and 6×10^{-12} cm W^{-1} for ImCuPc and ImZnPc, respectively.[23] For the phthalocyanines pc1 and pc2, the values of n_2 were found to be 5.6×10^{-16} and 11.4×10^{-16} cm^2 W^{-1}, and the values of α_3 were found to be 0.00091 and 0.00095 cm^3 GW^{-2}, respectively, by exciting at 800 nm using a 100 fs laser pulse.[24] Even the NLO parameter values obtained in this work are found to be better than those

of other organic systems. $n_2 = 3.4 \times 10^{-16}$ cm^2 W^{-1} was obtained for novel porphycenes (OAPo-T) by exciting the sample with a femtosecond laser pulse at 800 nm.[61] For phosphorus(v) corroles,[62] the obtained values of β were $(2.4–4.6) \times 10^{-13}$ cm W^{-1}. For porphyrins,[28] the obtained values of α_3 were in the range of $(2.34–2.68) \times 10^{-5}$ cm^3 GW^{-2}. Lin *et al.*[63] studied degenerate 3PA for D−π−A-based molecules having two identical electron-pulling moieties, and they observed the value of α_3 to be $\sim 3.85 \times 10^{-6}$ cm^3 GW^{-2}. Clearly, the calculated NLO coefficients of these metal substituted phthalocyanines are comparable to and higher than the NLO parameters of similar material systems, indicating prospects of these Pcs as an important group of NLO materials.

A convenient way to measure a system's effectiveness in terms of if application potential is to calculate the figure of merit (FOM). We obtained the nonlinear FOM[64,65] for these Pcs to show their potential for photonic switching applications. A low nonlinear absorption and a higher n_2 are appropriate for optical switching applications. The FOM is associated with the maximum nonlinear phase shift (NPS). The NPS will be limited if nonlinear losses predominate in materials with potent multiphoton absorption. Then, for 3PA, the absorption depth can be described as $(I_0^2\alpha_3)^{-1}$, where I_0 is the peak intensity of light. The corresponding figures of merit (FOMs) are defined as

$$V^{-1} = \frac{3n_2}{I_0\alpha_3\lambda}, \qquad (9)$$

where $V < 0.68$ is the condition[65,66] that must be satisfied to acquire a nominal nonlinear phase shift of 2π for switching, in order to operate properly a photonic device built of such materials. Our calculated values of V were 0.67 for H$_2$-TIPc, 0.43 for Zn-TIPc and 0.59 for Cu-TIPc. It is noteworthy that, although the condition $V < 0.68$ is satisfied for all of the Pcs investigated here, better results were found for the metallated Pcs. Gu *et al.*[66] have recently reported the value of V to be 0.64 for chalcone derivatives. Previously, for an input intensity of 230 GW cm^{-2}, we reported values of V as 0.57 and 0.59 for two phthalocyanine molecules, pc1 and pc2, respectively.[67] Evidently, the metal-substituted Pcs discussed here show the best photonic switching application compared with that of other material systems.

Conclusions

A thorough investigation of the photophysical properties, ultrafast excited-state dynamics and NLO characteristics of novel imidazole phthalocyanines is presented *via* a combined study of steady-state absorption and photoluminescence, time-resolved photoluminescence, electrochemical testing, DFT/TD-DFT, visible probe fs-TAS and fs Z-scan measurements. Due to the presence of an imidazole group, the molecules showed a wide Soret band, whilst their metal phthalocyanine group was responsible for their distinctive Q-bands. The target model analysis of fs-TAS was employed to obtain the decay times of various excited states and the corresponding rate constants. The longer decay components of the metallated Pcs were ascribed to the abundant charge flow from the metal centers and large spin–orbit coupling. The distinct decay process of Cu-TIPc was noted to be due to the presence of a tripdoublet state. A large two-photon absorption cross-section (8.89×10^{-47} cm^4 s for Cu-TIPc) and a three-photon absorption cross-section (9.65×10^{-77} cm^6 s^2) were extracted from theoretical fitting to the experimental Z-scan data using the three-level rate equations. In addition, we obtained very high values of the nonlinear refractive index and second hyperpolarizability ($\sim 10^{-30}$ esu) (also verified *via* DFT/TD-DFT calculations) for these Pcs, and were found to be superior to the previously reported values of similar molecules. An enhancement of the NLO parameters was observed for the metallated Pcs due to a reduction of the aggregation effect. Furthermore, the calculated values of the optical-limiting onset and FOM were excellent, and we conclude that these Pcs will draw particular attention for optical-limiting and photonic-switching applications. The investigations performed in this report exposed the multifunctionality of potential material systems. By contrast, a correlation between the fundamental optical properties of metallated Pcs with their various nonlinear optoelectronic applications was revealed.

Conflicts of interest

There are no conflicts to declare.

Acknowledgements

References

1 T. C. Parker, D. G. D. Patel, K. Moudgil, S. Barlow, C. Risko, J.-L. Brédas, J. R. Reynolds and S. R. Marder, Heteroannulated acceptors based on benzothiadiazole, *Mater. Horiz.*, 2015, **2**, 22–36.

2 Y. Li, M. Gu, Z. Pan, B. Zhang, X. Yang, J. Gu and Y. Chen, Indacenodithiophene: a promising building block for high performance polymer solar cells, *J. Mater. Chem. A*, 2017, **5**, 10798–10814.

3 Y. Li, K. Yao, H. L. Yip, F. Z. Ding, Y. X. Xu, X. Li, Y. Chen and A. K. Y. Jen, Eleven-Membered Fused-Ring Low Band-Gap Polymer with Enhanced Charge Carrier Mobility and Photovoltaic Performance, *Adv. Funct. Mater.*, 2014, **24**, 3631–3638.

4 J. Cao, Q. Liao, X. Du, J. Chen, Z. Xiao, Q. Zuo and L. Ding, A pentacyclic aromatic lactam building block for efficient polymer solar cells, *Energy Environ. Sci.*, 2013, **6**, 3224–3228.

5 W. Wu, R. Tang, Q. Li and Z. Li, Functional hyperbranched polymers with advanced optical, electrical and magnetic properties, *Chem. Soc. Rev.*, 2015, **44**, 3997–4022.

6 E. Rezaee, D. Khan, S. Cai, L. Dong, H. Xiao, S. R. P. Silva, X. Liu and Z.-X. Xu, Phthalocyanine in perovskite solar cells: a review, *Mater. Chem. Front.*, 2023, **7**, 1704–1736.

7 M. Pegu, D. Molina, M. J. Álvaro-Martins, M. Castillo, L. Ferrer, P. Huang, S. Kazim, Á. Sastre-Santos and S. Ahmad, Dimers of diethynyl-conjugated zinc-phthalocyanine as hole selective layers for perovskite solar cell fabrication, *J. Mater. Chem. C*, 2022, **10**, 11975–11982.

8 S. Bhattacharya, C. Biswas, S. S. K. Raavi, J. V. S. Krishna, D. Koteshwar, L. Giribabu and S. V. Rao, Optoelectronic, femtosecond nonlinear optical properties and excited state dynamics of a triphenyl imidazole induced phthalocyanine derivative, *RSC Adv.*, 2019, **9**, 36726–36741.

9 D.-J. Li, Q.-h Li, Z.-R. Wang, Z.-Z. Ma, Z.-G. Gu and J. Zhang, Interpenetrated metal-porphyrinic framework for enhanced nonlinear optical limiting, *J. Am. Chem. Soc.*, 2021, **143**, 17162–17169.

10 R. Xu, M. Zhu, W. Li, J. Ding and Y. Zhang, Excellent Nonlinear Optical Limiting Behavior of Tetra (C60) Lanthanum Phthalocyanine in Solid Poly (methyl methacrylate) Films, *J. Phys. Chem. C*, 2023, **127**, 4258–4265.

11 B. P. Biswal, S. Valligatla, M. Wang, T. Banerjee, N. A. Saad, B. M. K. Mariserla, N. Chandrasekhar, D. Becker, M. Addicoat and I. Senkovska, Nonlinear optical switching in regioregular porphyrin covalent organic frameworks, *Angew. Chem., Int. Ed.*, 2019, **58**, 6896–6900.

12 R. U. Khan, O. P. Kwon, A. Tapponnier, A. N. Rashid and P. Günter, Supramolecular ordered organic thin films for nonlinear optical and optoelectronic applications, *Adv. Funct. Mater.*, 2006, **16**, 180–188.

13 G. De La Torre, P. Vázquez, F. Agullo-Lopez and T. Torres, Role of structural factors in the nonlinear optical properties of phthalocyanines and related compounds, *Chem. Rev.*, 2004, **104**, 3723–3750.

14 H. Abramczyk and I. Szymczyk, Aggregation of phthalocyanine derivatives in liquid solutions and human blood, *J. Mol. Liq.*, 2004, **110**, 51–56.

15 A. J. Pearson, T. Plint, S. T. Jones, B. H. Lessard, D. Credgington, T. P. Bender and N. C. Greenham, Silicon phthalocyanines as dopant red emitters for efficient solution processed OLEDs, *J. Mater. Chem. C*, 2017, **5**, 12688–12698.

16 E. Nouri, J. V. S. Krishna, C. V. Kumar, V. Dracopoulos, L. Giribabu, M. R. Mohammadi and P. Lianos, Soluble

tetratriphenylamine Zn phthalocyanine as hole transporting material for perovskite solar cells, *Electrochim. Acta*, 2016, **222**, 875–880.

17 Y. Chen, M. Hanack, W. J. Blau, D. Dini, Y. Liu, Y. Lin and J. Bai, Soluble axially substituted phthalocyanines: Synthesis and nonlinear optical response, *J. Mater. Sci.*, 2006, **41**, 2169–2185.

18 S. Bhattacharya, C. Biswas, S. S. K. Raavi, J. Venkata Suman Krishna, N. Vamsi Krishna, L. Giribabu and V. R. Soma, Synthesis, optical, electrochemical, DFT studies, NLO properties, and ultrafast excited state dynamics of carbazole-induced phthalocyanine derivatives, *J. Phys. Chem. C*, 2019, **123**, 11118–11133.

19 J. Follana-Berná, R. Farran, W. Leibl, A. Quaranta, Á. Sastre-Santos and A. Aukauloo, Phthalocyanine as a Bioinspired Model for Chlorophyll f-Containing Photosystem II Drives Photosynthesis into the Far-Red Region, *Angew. Chem., Int. Ed.*, 2021, **60**, 12284–12288.

20 Z. Liu, B. Zhang, N. Dong, J. Wang and Y. Chen, Perfluorinated gallium phthalocyanine axially grafted black phosphorus nanosheets for optical limiting, *J. Mater. Chem. C*, 2020, **8**, 10197–10203.

21 D. Mwanza, M. Louzada, J. Britton, E. Sekhosana, S. Khene, T. Nyokong and P. Mashazi, The effect of the cobalt and manganese central metal ions on the nonlinear optical properties of tetra (4-propargyloxyphenoxy) phthalocyanines, *New J. Chem.*, 2018, **42**, 9857–9864.

22 P. Zhao, Z. Wang, J. Chen, Y. Zhou and F. Zhang, Nonlinear optical and optical limiting properties of polymeric carboxyl phthalocyanine coordinated with rare earth atom, *Opt. Mater.*, 2017, **66**, 98–105.

23 S. Bhattacharya, G. Reddy, S. Paul, S. S. Hossain, S. S. K. Raavi, L. Giribabu, A. Samanta and V. R. Soma, Comparative photophysical and femtosecond third-order nonlinear optical properties of novel imidazole substituted metal phthalocyanines, *Dyes Pigm.*, 2021, **184**, 108791.

24 R. S. S. Kumar, S. V. Rao, L. Giribabu and D. N. Rao, Femtosecond and nanosecond nonlinear optical properties of alkyl phthalocyanines studied using Z-scan technique, *Chem. Phys. Lett.*, 2007, **447**, 274–278.

25 M. J. Frisch, G. W. Trucks, H. B. Schlegel, G. E. Scuseria, M. A. Robb, J. R. Cheeseman, G. Scalmani, V. Barone, G. A. Petersson, H. Nakatsuji, X. Li, M. Caricato, A. V. Marenich, J. Bloino, B. G. Janesko, R. Gomperts, B. Mennucci, H. P. Hratchian, J. V. Ortiz, A. F. Izmaylov, J. L. Sonnenberg, D. Williams-Young, F. Ding, F. Lipparini, F. Egidi, J. Goings, B. Peng, A. Petrone, T. Henderson, D. Ranasinghe, V. G. Zakrzewski, J. Gao, N. Rega, G. Zheng, W. Liang, M. Hada, M. Ehara, K. Toyota, R. Fukuda, J. Hasegawa, M. Ishida, T. Nakajima, Y. Honda, O. Kitao, H. Nakai, T. Vreven, K. Throssell, J. A. Montgomery Jr., J. E. Peralta, F. Ogliaro, M. J. Bearpark, J. J. Heyd, E. N. Brothers, K. N. Kudin, V. N. Staroverov, T. A. Keith, R. Kobayashi, J. Normand, K. Raghavachari, A. P. Rendell, J. C. Burant, S. S. Iyengar, J. Tomasi, M. Cossi, J. M. Millam, M. Klene, C. Adamo, R. Cammi, J. W. Ochterski, R. L. Martin, K. Morokuma, O. Farkas, J. B. Foresman and D. J. Fox, *Gaussian 16 Rev. C.01*, 2016.

26 I. H. Van Stokkum, B. Van Oort, F. Van Mourik, B. Gobets and H. Van Amerongen, (Sub)-picosecond spectral evolution of fluorescence studied with a synchroscan streak-camera system and target analysis, *Biophysical techniques in photosynthesis*, 2008, pp. 223–240.

27 C. Biswas, N. K. Katturi, N. Duvva, L. Giribabu, V. R. Soma and S. S. K. Raavi, Multistep electron injection dynamics and optical nonlinearity investigations of π-extended thioalkyl-substituted tetrathiafulvalene sensitizers, *J. Phys. Chem. C*, 2020, **124**, 24039–24051.

28 M. S. Ahmed, C. Biswas, B. Bhavani, S. Prasanthkumar, D. Banerjee, V. Kumar, P. Chetti, L. Giribabu, V. R. Soma and S. S. K. Raavi, Metalated porphyrin-napthalimide based donor-acceptor systems with long-lived triplet states and effective three-photon absorption, *J. Photochem. Photobiol., A*, 2023, **435**, 114324.

29 D. Banerjee, S. S. B. Moram, C. Byram, J. Rathod, T. Jena, G. K. Podagatlapalli and V. R. Soma, Plasmon-enhanced ultrafast and tunable thermo-optic nonlinear optical properties of femtosecond laser ablated TiO_2 and Silver-doped TiO_2 nanoparticles, *Appl. Surf. Sci.*, 2021, **569**, 151070.

30 M. S. Ahmed, L. Sireesha, S. K. Nayak, R. Bakthavatsalam, D. Banerjee, V. R. Soma, J. Kundu and S. S. K. Raavi, Tunable near-infrared emission and three-photon absorption in lanthanide-doped double perovskite nanocrystals, *Nanoscale*, 2023, **15**, 9372–9389.

31 M. S. Ahmed, S. K. Nayak, L. Sireesha, J. Rathod, V. R. Soma and S. S. K. Raavi, Enhanced femtosecond nonlinear optical response in Mn-doped $Cs_2AgInCl_6$ nanocrystals, *Opt. Lett.*, 2023, **48**, 3519–3522.

32 A. Patel, S. Y. Sharp, K. Hall, W. Lewis, M. F. Stevens, P. Workman and C. J. Moody, Fused imidazoles as potential chemical scaffolds for inhibition of heat shock protein 70 and induction of apoptosis. Synthesis and biological evaluation of phenanthro [9, 10-d] imidazoles and imidazo [4, 5-f][1, 10] phenanthrolines, *Org. Biomol. Chem.*, 2016, **14**, 3889–3905.

33 L. Giribabu, N. Duvva, S. P. Singh, L. Han, I. M. Bedja, R. K. Gupta and A. Islam, Stable and charge recombination minimized π-extended thioalkyl substituted tetrathiafulvalene dye-sensitized solar cells, *Mater. Chem. Front.*, 2017, **1**, 460–467.

34 W. Zheng, B.-B. Wang, J.-C. Lai, C.-Z. Wan, X.-R. Lu, C.-H. Li and X.-Z. You, Electrochromic properties of novel octa-pinene substituted double-decker Ln (III)(Ln= Eu, Er, Lu) phthalocyanines with distinctive near-IR absorption, *J. Mater. Chem. C*, 2015, **3**, 3072–3080.

35 D. Koteshwar, S. Prasanthkumar, S. P. Singh, T. H. Chowdhury, I. Bedja, A. Islam and L. Giribabu, Effects of methoxy group (s) on D-π-A porphyrin based DSSCs: efficiency enhanced by co-sensitization, *Mater. Chem. Front.*, 2022, **6**, 580–592.

36 A. Koca, Spectroelectrochemistry of phthalocyanines, Electrochemistry of N4 Macrocyclic Metal Complexes, *Biomimesis, Electroanalysis and Electrosynthesis of MN4 Metal Complexes*, 2016, vol. 2, pp. 135–200.

37 S. Bharanidharan and P. Myvizhi, Frontier molecular orbitals (FMO) and molecular electrostatic potential (MEP) surface of 2-(4-chlorophenyl)-1-((furan-2-yl) methyl)-4, 5-dimethyl-1H-imidazole using DFT method, *Int J. Pure Appl. Math.*, 2018, **119**, 6769–6777.

38 I. H. van Stokkum, D. S. Larsen and R. Van Grondelle, Global and target analysis of time-resolved spectra, *Biochim. Biophys. Acta*, 2004, **1657**, 82–104.

39 J. J. Snellenburg, S. Laptenok, R. Seger, K. M. Mullen and I. H. van Stokkum, Glotaran: A Java-based graphical user interface for the R package TIMP, *J. Stat. Software*, 2012, **49**, 1–22.

40 I. H. Van Stokkum, B. V. Oort, F. V. Mourik, B. Gobets and H. V. Amerongen, in *Biophysical techniques in photosynthesis*, Springer, 2008, pp. 223–240.

41 X. Zheng, Y. Wang, J. Hu, G. Yang, Z. Guo, J. Xia, Z. Xu and G. Fang, Octamethyl-substituted Pd(II) phthalocyanine with long carrier lifetime as a dopant-free hole selective material for performance enhancement of perovskite solar cells, *J. Mater. Chem. A*, 2017, **5**, 24416–24424.

42 T. Tran-Thi, J. Lipskier, D. Houde, C. Pepin, E. Keszei and J. Jay-Gerin, Subpicosecond excitation of strongly coupled porphyrin–phthalocyanine mixed dimers, *J. Chem. Soc., Faraday Trans.*, 1992, **88**, 2129–2137.

43 M. Fournier, C. Pépin, D. Houde, R. Ouellet and J. E. van Lier, Ultrafast studies of the excited-state dynamics of copper and nickel phthalocyanine tetrasulfonates: potential sensitizers for the two-photon photodynamic therapy of tumors, *Photochem. Photobiol. Sci.*, 2004, **3**, 120–126.

44 P. Huang, A. Hernandez, S. Kazim, J. Follana-Berna, J. Ortiz, L. Lezama, A. Sastre-Santos and S. Ahmad, Asymmetrically substituted phthalocyanines as dopant-free hole selective layers for reliability in perovskite solar cells, *ACS Appl. Energy Mater.*, 2021, **4**, 10124–10135.

45 G. De La Torre, M. Nicolau and T. Torres, *Supramolecular photosensitive and electroactive materials*, Elsevier, 2001, pp. 1–111.

46 S. K. Nayak, R. Kore, M. S. Ahmed, P. Verma, R. Vallavoju, D. Banerjee, S. Pola, V. R. Soma, P. Chetti and S. S. K. Raavi, Femtosecond nonlinear optical properties of polycyclic aromatic hydrocarbon-based Benzo [e] pyrene derivatives, *Optic. Mater.*, 2023, **137**, 113603.

47 N. G. Horton, K. Wang, D. Kobat, C. G. Clark, F. W. Wise, C. B. Schaffer and C. Xu, In vivo three-photon microscopy of subcortical structures within an intact mouse brain, *Nat. Photonics*, 2013, **7**, 205–209.

48 Q. Zheng, G. S. He, C. Lu and P. N. Prasad, Synthesis, two- and three-photon absorption, and optical limiting properties of fluorene-containing ferrocene derivatives, *J. Mater. Chem.*, 2005, **15**, 3488–3493.

49 P. Patil, S. R. Maidur, S. V. Rao and S. Dharmaprakash, Crystalline perfection, third-order nonlinear optical properties and optical limiting studies of 3, 4-Dimethoxy-4′-methoxychalcone single crystal, *Opt. Laser Technol.*, 2016, **81**, 70–76.

50 R. L. Sutherland, *Handbook of nonlinear optics*, CRC press, 2003.

51 M. S. Ahmed, C. Biswas, D. Banerjee, P. Chetti, J.-S. Yang, V. R. Soma and S. S. K. Raavi, Femtosecond Third-Order Non-Linear Optical Properties of Unconstrained Green Fluorescence Protein Chromophores, *Front. Phys.*, 2022, 549.

52 C. Biswas, P. S. Gangadhar, L. Giribabu, P. Chetti, D. Banerjee, V. R. Soma and S. S. K. Raavi, Ultrafast intramolecular charge transfer dynamics and nonlinear optical properties of phenothiazine-based push–pull zinc porphyrin, *J. Photochem. Photobiol., A*, 2022, **433**, 114141.

53 L. Polavarapu, Q.-H. Xu, M. S. Dhoni and W. Ji, Optical limiting properties of silver nanoprisms, *Appl. Phys. Lett.*, 2008, **92**, 263110.

54 L. Polavarapu, N. Venkatram, W. Ji and Q.-H. Xu, Optical-limiting properties of oleylamine-capped gold nanoparticles for both femtosecond and nanosecond laser pulses, *ACS Appl. Mater. Interfaces*, 2009, **1**, 2298–2303.

55 R. Wei, X. Tian, Z. Hu, H. Zhang, T. Qiao, X. He, Q. Chen, Z. Chen and J. Qiu, Vertically standing layered MoS_2 nanosheets on TiO_2 nanofibers for enhanced nonlinear optical property, *Opt. Express*, 2016, **24**, 25337–25344.

56 M. S. Ahmed, C. Biswas, P. B. Miranda and S. S. K. Raavi, Nonlinear optical techniques for characterization of organic electronic and photonic devices, *Eur. Phys. J.: Spec. Top.*, 2021, 1–17.

57 R. W. Boyd, *Nonlinear optics*, Academic Press, 2020.

58 M. Sheik-Bahae, A. A. Said, T.-H. Wei, D. J. Hagan and E. W. Van Stryland, Sensitive measurement of optical nonlinearities using a single beam, *IEEE J. Quantum Electron.*, 1990, **26**, 760–769.

59 C. Prabhakar, K. Yesudas, K. Bhanuprakash, V. J. Rao, R. S. Santosh Kumar and D. N. Rao, Linear and nonlinear optical properties of mesoionic oxyallyl derivatives: enhanced non-resonant third order optical nonlinearity in croconate dyes, *J. Phys. Chem. C*, 2008, **112**, 13272–13280.

60 C. Prabhakar, K. Bhanuprakash, V. J. Rao, M. Balamuralikrishna and D. N. Rao, Third order nonlinear optical properties of squaraine dyes having absorption below 500 nm: a combined experimental and theoretical investigation of closed shell oxyallyl derivatives, *J. Phys. Chem. C*, 2010, **114**, 6077–6089.

61 N. N. Pati, S. Sahoo, S. S. Sahoo, D. Banerjee, S. Venugopal Rao and P. K. Panda, Chromatographically separable ruffled non-planar isomeric octaalkylporphycenes: consequences of unsymmetrical substitution upon structure and photophysical properties, *New J. Chem.*, 2020, **44**, 9616–9620.

62 N. K. Katturi, S. A. Balahoju, A. Ramya, C. Biswas, S. S. K. Raavi, L. Giribabu and V. R. Soma, Ultrafast photophysical and nonlinear optical properties of novel free base and axially substituted phosphorus (V) corroles, *J. Mol. Liq.*, 2020, **311**, 113308.

63 T.-C. Lin, G. S. He, Q. Zheng and P. N. Prasad, Degenerate two-/three-photon absorption and optical power-limiting properties in femtosecond regime of a multi-branched chromophore, *J. Mater. Chem.*, 2006, **16**, 2490–2498.

64 F. Gholami, S. Zlatanovic, A. Simic, L. Liu, D. Borlaug, N. Alic, M. P. Nezhad, Y. Fainman and S. Radic, Third-order nonlinearity in silicon beyond 2350 nm, *Appl. Phys. Lett.*, 2011, **99**, 081102.

65 J. U. Kang, A. Villeneuve, M. Sheik-Bahae, G. I. Stegeman, K. Al-hemyari, J. S. Aitchison and C. N. Ironside, Limitation due to three-photon absorption on the useful spectral range

for nonlinear optics in AlGaAs below half band gap, *Appl. Phys. Lett.*, 1994, **65**, 147–149.

66 B. Gu, W. Ji, P. Patil and S. Dharmaprakash, Ultrafast optical nonlinearities and figures of merit in acceptor-substituted 3, 4, 5-trimethoxy chalcone derivatives: Structure-property relationships, *J. Appl. Phys.*, 2008, **103**, 103511.

67 R. S. S. Kumar, S. V. Rao, L. Giribabu and D. N. Rao, Ultrafast nonlinear optical properties of alkyl phthalocyanines investigated using degenerate four-wave mixing technique, *Optic. Mater.*, 2009, **31**, 1042–1047.